Nitrogen-phosphorous co-doped porous carbon from cross-linked polymers for supercapacitor applications

Daba T. Bakhoum [a], Ndeye F. Sylla [a], Samba Sarr [a], Vusani M. Maphiri [a], Ndeye M. Ndiaye [b], Delvina J. Tarimo [a], Astou Seck [c], Balla D. Ngom [b], Mohamed Chaker [c] and Ncholu Manyala [a*]

[a] Department of Physics, University of Pretoria, Pretoria 0028, South Africa

[b] Laboratoire de Photonique Quantique, d'Energie et de Nano-Fabrication, Faculté des Sciences et Techniques Université Cheikh Anta Diop de Dakar (UCAD) B.P. 5005 Dakar-Fann Dakar, Sénégal

[c] Institut National de la Recherche Scientifique Centre—Énergie Matériaux Télécommunications 1650, Boulevard Lionel Boulet, Varennes, QC J3X 1S2, Canada

*Corresponding author's email: ncholu.manyala@up.ac.za, Tel.: + (27)12 420 3549, Fax: + (27)12 420 2516

Abstract

Herein, we report co-doped porous carbon with nitrogen-phosphorous derived from cross-linked polyvinyl alcohol and polyvinylpyrrolidone (AC-PA/PP/AP-x) polymers synthesized using a simple single activation process. Diammonium hydrogen phosphate (AP) acting as nitrogen and phosphorous source was used to dope the cross-linked polymer precursors. The properties of the as synthesised carbon materials were analysed using the following techniques: scanning electron microscopy (SEM), X-ray photoelectron spectroscopy (XPS), powder X-ray diffraction (XRD), Energy-dispersive X-ray spectroscopy (EDS) mapping, Raman spectroscopy and nitrogen sorption isotherm. The optimized AC-PA/PP/AP-0.5 sample possess the highest porous surface properties i.e., specific surface area (2656 $m^2\,g^{-1}$), pore volume (1.08 $cm^3\,g^{-1}$) and micropore volume (0.99 $cm^3\,g^{-1}$). The sample also achieved a remarkable specific capacitance ($252\,F\,g^{-1}$) corresponding to a specific current of $1\,A\,g^{-1}$ measured within the presence of 2.5 M KNO_3 aqueous electrolyte, in three electrode set-up. The constructed symmetric AC-PA/PP/AP-0.5//AC-PA/PP/AP-0.5 SC with a good electrical series resistance (ESR=0.6 Ω), delivers a great specific energy (27.3 W h kg^{-1}) and specific power (400 W kg^{-1}) when monitoring at $0.5\,A\,g^{-1}$ using same electrolyte. Good

capacitance retention of 90 % was obtained while charge-discharging (CD) the device for about 10,000 cycles at 5 $A\ g^{-1}$. The CD cycling also yielded a coulombic efficiency of 99.8%. Thus, this porous carbon produced via cross-linking and heteroatom doping, has a well-connected hierarchical porous structure that includes both micropores and mesopores. This structure is important for charge storage and transport. Therefore, the fabricated symmetric cell is a promising supercapacitor energy storage device, where a high power is requisite.

Keywords: Supercapacitor; N, P co-doped; Heteroatom; Polymers; Activated carbon.

1.Introduction

The skyrocketing progress - development of electric automobile and endless mobile electronics; and the ever-increasing world population have induced the high energy demand and an abundant consumption of non-renewable energy [1][2]. Fossil fuels provide most of the worldwide energy and this is causing their depletion. Even worse, they pollute the atmosphere and destroys our ozone layer. Greenhouse gases emissions induce global warming and climate change which cause health, ecological and environmental issues [3][4]. To face it all, researchers are challenged to find pioneering ideas implying the development of green suitable energy. Thus, many researchers are focused on the utilisation of renewable energy sources: tidal, solar and wind energy which has to be coupled to an energy storage device whereby the generated energy can be stored and used as needed [5][6]. As a novel electrochemical device that bridges the gap between traditional capacitor and batteries, supercapacitors (SCs) have received increasing attention [7]. They have long cycle life, ultra-charge-discharge (GD) ability, high power and lacks high energy and also prone to self-discharge [8][6]. These drawbacks hinder their broad commercial application. This has challenged researchers to better

the energy of SCs while retaining other preparties [5]. These devices can be classified into two categories i.e., pseudocapacitors (PCs) and electrical double layer capacitors (EDLCs) -based on the charge storage mechanism. EDLCs accumulate charges within the electrode/electrolyte interface through an electrostatic charge adhesion. Involving a reversible and rapid-redox reaction, PCs store charge at the electrode surface. There are hybrid capacitors which combine both EDLCs and PCs materials characteristics [9][10]. Moreover, carbon-based material possesses EDLCs behaviour and due to their large specific surface area, great stability, easily tuned morphology, good electrical conductivity, they can deliver a large specific capacitance [11][12]. On the other hand, conducting polymers, transition metal oxide/hydroxide are common materials adopted for PCs [13]. These materials provide high specific capacity but have a major hurdle of low conductivity [10].

A larger range of nanostructured carbon materials (nanotubes, nanosheets, nanofibers) have found widespread use. They are synthesized using different carbon sources such as biomass [14][15], metal-organic frameworks [16][17] and polymers [18][19]. Among them activated carbon (AC) obtained from polymers have gain attention due to their well-developed and interconnected-pore network which is crucial for ion diffusion/transport and EDLC enhancement. By utilizing well-defined starting materials, activated carbon from polymers can offer a viable alternative to conventional carbon [20]. A variety of activated carbon from polymer precursors such as polyvinylpyrrolidone (PP) [21], hypercrosslinked polymers (HCP) from divinylbenzene [22], and tetraphenylethene-conjugated porous organic polymer (TPE-CPOP) [23] have been reported as SCs electrode material.

Cross-linking polymers have strong links and predominant porosity. They have distinctive features such as mild operating condition, low cost and easy functionalization leading to a better electrochemical performance. The cross-linking provides a large SSA for the accommodation of the electrolyte ions and its architecture allows the fast transfer and diffusion

of the ions [24][25]. However, in order to fulfil the rising energy demand, porous carbon from polymers need to be electrochemical enhanced [26][27].

To date, numerous approaches of enhancing electrochemical performance of porous carbon has been reported. Approaches such as doping with heteroatom like nitrogen (N), phosphorous (P), boron (B), sulfur (S) and fluorine (F)) to promote surface activity and electrochemical performance [28][29]. Moreover, the presence of heteroatoms provides additional pseudocapacitive behaviour also alter the charge distribution of the carbon network. The active sites can be intensifying to access electrolytes through the carbon matrix. This facilitates the electrochemical reaction at the interface [30][31]. Among the listed dopants, nitrogen is the most commonly used in activated carbon due to is ability to significantly increase electrical conductivity and also improve wettability [32][33][34]. On the other hand, incorporation of phosphorous can modify the electrochemical performance by changing the charge density and resulting in more disordered structures [35]. The capacity of P to prevent the occurrence of certain side effects including the oxidation of the electrode, has been shown to considerably enhance the cycle stability, potential window and then the specific energy. Also, it is well known that the pore size distribution (PSD) and pore volume are positively impacted by the presence of structures that contain P [36]. However, the combination of nitrogen and phosphorous have gained a lot of attention and demonstrated to be the most auspicious approach to enhance the capacitance of the carbon and maintains its good rate performance [37]. This is because the multi-doping provides more actives sites than the single doping because of synergistic effect from the heteroatoms that leads to an improved electrochemical performance [38]. Although, nitrogen and phosphorous have similar doping features, phosphorous provides more active sites for charge storage due to its larger radius [39]. Heteroatom-doped porous carbon has been repeatedly reported to have increased: conductivity, wettability, and charge storage capability of the electrode material. Ragavan et al. [40] reported

nitrogen and phosphorous co-doped mesoporous carbon using a chemical vapor deposition nanocasting using aniline, phenol and triphenylphosphine as sources for nitrogen, carbon and phosphorous respectively. The study indicated that N, P co-doped has the highest specific capacitance of $355\,F\,g^{-1}$ compared to $303\,F\,g^{-1}$ (P-doped), $208\,F\,g^{-1}$ (N-doped) and $166\,F\,g^{-1}$ (undoped) while measuring at $0.5\,A\,g^{-1}$. The augmentation in specific capacitance was influenced by the additional of pseudocapacitance from heteroatoms. Their work revealed that the type and the amount of the dopant affect the electrical conductivity and the degree of disorder which boost the electrochemical performance. On the other hand, multi-doped carbon from cross-linked polymers have gained important attention due to their interconnected hierarchical well-developed porous structure for ion electrolyte transport. Several authors such as Li et al. [41] and Zhu et al. [42] have both reported heteroatoms N, P co-doped carbon-based materials. Ref [41] illustrate doped from cross-linking cyclophosphazene produced by carbonisation followed by KOH activation and this material showed a specific energy and power of 14.912 Wh kg^{-1} and 800 W kg^{-1}. Whereas Ref [42] reports doped cross-linked carbon nanofibers using polyaniline (PANI) as a source of carbon which displayed a specific energy and power of 27.70 W h kg^{-1} and 231.08 kW kg^{-1}. Lastly, Yang et al. [43] prepared a symmetric SC which was fabricated from a cross-linked polyphosphazenes, and the assembled cell exhibited 9.13 W h kg^{-1} specific energy at 0.5 A g^{-1} and specific power of 123.7 kW kg^{-1}. These reports demonstrate that morphology and structure of the material can be tuned by cross-linking doped polymer which enhance the electrochemical performance. However, for all these examples, the authors have used a long processes or lot of precursors to synthesis their co-doped carbon.

In this work, we are focusing on one step nitrogen (N) and phosphorous (P) co-doping of the cross-linked polymers polyvinyl alcohol and polyvinyl pyrrolidone (PA/PP) using

diammonium hydrogen phosphate as dopant sources, in order to obtain high porous activated carbon with well-defined interconnected pores. In our best knowledge, it is the first work on a co-doped polymer from PA/PP as carbon source using diammonium phosphate (AP) as both nitrogen and phosphorous sources to produce the N and P electrodes denoted as PA/PP/AP-x, where x represents the relative amount of AP used. A simple mechanism is used to fabricate the activated carbon: (1) Hydrothermal method to obtain the PA/PP powder cross-linked polymer, and (2) one step co-doping and activation of the cross-linked polymers. This study provides a new simple pathway to produce an environmentally, relatively low-cost heteroatoms doped ACs from crosslinked polymers which can be an alternative to the conventional ACs for electrochemical capacitors devices. The SC performance of the prepared material was evaluated using 2.5 molar potassium nitrate aqueous electrolyte (2.5M KNO_3). Effect of the dopant agent/hydrochar [44] ratio on the electrochemical behaviour was carried out. AC-PA/PP/AP-0.5 showed higher electrochemical behaviour, which was subsequently used in symmetric SC device. The SC device showed a good electrochemical stability as suggest by floating measurement and also displays a specific energy and power of 27.3 W h kg^{-1} and 400 kW kg^{-1} at specific current 0.5 $A\ g^{-1}$ within a wide operating cell potential.

2. Experimental section

2.1. Sample preparation

2.1.1. PA/PP cross-link powder preparation

The PA/PP cross-linked powder was synthesized similarly to our previously work [44]. In summary, 10 g and 2.5 g of PVA (molecular weight: 89,000-98,000) and PVP (molecular weight: 10,000) were mixed within 100 mL of deionized (DI) water. Then continuously stirred for 2 h under a constant supply of heat at 80 °C to obtain a gel-polymer. Subsequently, the gel-polymer was transferred into a Teflon-lined stainless-steel autoclave which was also transferred

into an electric oven then heated at 180 °C for 14 h as illustrated in scheme 1(a). After cooling down, the yellow solid was crashed and thoroughly cleaned with DI water then finally dried in an electric oven at 60 °C for overnight.

2.1.2 Preparation of AC-PA and AC-PA/PP/AP-x powders

The dried PA/PP yellow powder was mixed with AP ($(NH_4)_2HPO_4$) (molecular weight: 132) with different mass ratios 1:0.25; 1:0.5; 1:0.75 of PA/PP to AP and potassium hydroxide as seen in scheme 1(b). Potassium hydroxide was utilized as an activating agent. A mass ratio (weight of yellow powder: KOH) of 1:2 was chosen for the activation process. This ratio was optimized as detailed in our previous work [44]. The mix powder was placed inside the muffle and heated under the following conditions: 700 $^{\circ}$C for 2h at a heating rate of 5 $^{\circ}$C min^{-1}, under argon environment with a flow rate 300 standard cubic centimetre. This synthesis conditions were optimized in our previous work [45]. This process carbonized and also activated the carbon; and was repeated for each ratio of PA/PA to AP, co-doped activated samples were then denoted as AC-PA/PP/AP-X; x is the ratio of AP in the samples. For comparison the activated carbon without AP was also synthesised and labelled as AC-PA/PP. These AC samples were washed thoroughly with DI water to neutralize and remove the remaining activating agent. Then, finally dried at 60 °C in an electrical oven for overnight for further characterizations.

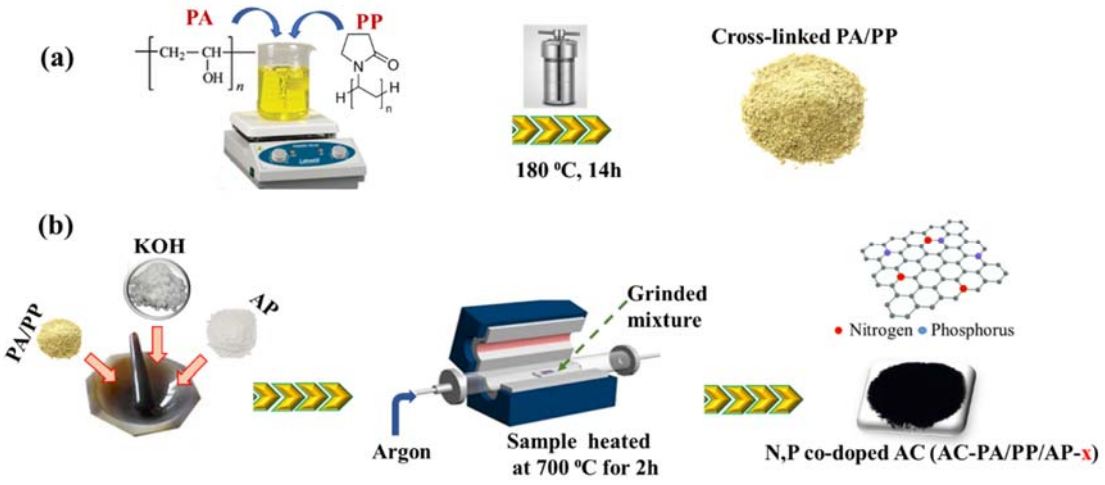

Scheme 1. Synthesis route of (a) cross-linked PA/PP powder and (b) AC-PA/PP/AP-x samples.

2.2 Material characterization

X-ray diffraction measurements were recorded by an XRD-Bruker D8 Advance (Panalytical, Netherlands), with a Cu K_α radiation source (λ = 0.1542 nm). The XRD was used to study the phase structures of the as-prepared samples in the reflection geometry at 2θ values (10–80°). Raman spectra were obtained using a WITec alpha 300 RAS+ Confocal micro-Raman microscope (Focus Innovations, Ulm, Germany) operated at 5 mW, 180 s and 532 nm for laser power, spectral acquisition time and laser wavelength, respectively. Zeiss Ultra plus 55 (Akishima-shi, Japan) field emission scanning electron microscopes (FE-SEM) operated at an accelerating voltage of 2.0 kV coupled with energy-dispersive X-ray spectroscopy (EDS) operated at 15.0 kV was used to characterize the surface morphology and elemental analysis of the synthesized samples. The porous structures were analysed by the nitrogen adsorption-desorption isotherms using NOVATOUCH built-in with a quantachrome (NOVA touch NT 2LX-1, Volts 220, USA) TouchWin software Version: 1.22. The samples were degassed at 150 °C for 8 h, in presence of high vacuum environment. The specific surface area was

calculated according to the Brunauer-Emmett-Teller (BET) technique in the relative pressure range (P/Po) of 0.01-0.3. The pore size distribution was assessed using a density function theory (DFT) software. The total pore volume was determined at a relative pressure of P/Po=0.95. The chemical composition of the samples was performed by X-ray photoelectron spectroscopy (XPS) using a VG Escalab 220i-XL instrument (Fisons instrument, UK) with a monochromatic Al-Kα (0.6 eV) source of radiation.

2.3 Electrochemical preparation and characterization

The electrodes were prepared as follows: 80 % of the active material (prepared activated carbon), 10 % acetylene carbon black and 10 % of polyvinylidene (PVDF as binder) were placed in a dish and few drops of N-methyl-2-pyrrolidone (NMP) were added to make a paste-like-slurry. The slurry was then coated on the nickel foam current collector and dried in an oven at 60 °C for overnight. The active material on the Ni foam was determined to be approximatively 2.3 mg cm^{-2} in the three electrode measurements. The mass per area of the single electrode in the device was ~ 2.5 mg cm^{-2} giving total mass of 5.0 mg cm^{-2} for the device. Ni foam was used as current collector in this study because of its high electrocatalytic activity, excellent stability, good electrical conductivity.as compared to some current collector such as, stainless steel and graphitic paper [29].

Electrochemical measurements were performed in both three-electrode and two-electrode configuration. The nickel foam coated electrode, Ag/AgCl and glassy carbon served as a working electrode, reference, and counter electrodes respectively. The 2.5 M KNO_3 electrolyte was used in both three- and two-electrode measurements. The electrolyte was optimized as seen in Fig. S1. The current response of AC-PA/PP in 2.5 M KNO_3 at 50 mV s^{-1} is higher than the other electrolytes, as displayed in Fig. S1 (a). The specific capacitances of AC-PA/PP (Fig. S1 (b)) at 1 A/g were determined to be 81, 91, 96, 122 and 170 F/g in 6 M KOH, 1 M Li_2SO_4,

1 M Na_2SO_4, 1 M KNO_3 and 2.5 M KNO_3 electrolytes, respectively. The following : Cyclic voltammetry (CV), galvanostatic charge discharge (GCD) and electrochemical impedance spectroscopy (EIS) electrochemical measurements were performed on an electrochemical workshop station (Bio-Logic VMP-300 potentiostat (Knoxville TN 37,930, USA) run using EC-Lab V11.33 software). The two-electrode measurements were contrived using a split cell with a filter paper separator.

3. Results and analysis

3.1. Structural, textural, and Morphological characterization

XRD and Raman were deployed to analyse the structural and vibrational properties of the as-prepared carbon materials. Fig. 1 (a) displays the XRD diffractometer of the prepared materials. All four patterns express two broad and weak diffractions at 23° and 43° indicating dominant characteristics of amorphous carbon material (relatively low degree of graphitization) [46]. The characteristic diffraction at 23° in the XRD patterns, assigned to the graphitic stacking of the (002) plan. The diffraction peak at 43° is analogous to the reflection of the (101) plane [47] which indicates the presence of graphitized structure. There was no any impurity peak detected for the samples. The XRD results confirms that the precursors are successfully transformed into carbon materials. As a result, all samples (AC-PA/PP/AP-x) have a disordered amorphous carbon structures, which are expected to provide excellent pore structures and charge storage capability [48].

Fig. 1 (b) illustrate the Raman spectrums of the prepared materials and it shows two distinct characteristic bands within the one phono range located at 1349 cm^{-1} (D band) and 1583 cm^{-1} (G band). D band corresponds to defects and disorder, while G band represents the ordered sp^2 carbon plane [49][50]. It can be seen that the intensity ratio of D to G band (I_D/I_G) reveals

carbon graphitization [49]. The incorporation of heteroatoms into the carbon framework increases the defects [40] in which the I_D/I_G increases with the amount of AP. The I_D/I_G for AC-PA/PP, AC-PA/PP/AP-0.25, AC-PA/PP/AP-0.5, AC-PA/PP/AP-0.75 samples are, 0.83, 0.85, 0.86 and 0.84, respectively as shown in Table S1. It can be seen that AC-PA/PP/AP-0.5 has more defect, suggesting better electrochemical performance [51][52]. More defects might suggest a good wettability for SCs. These results are in line with XRD results.

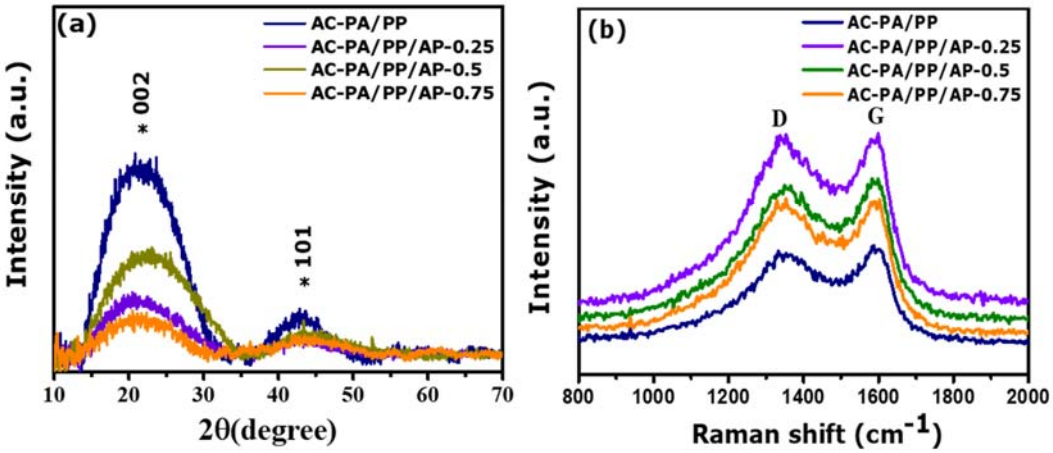

Fig. 1. (a) XRD and (b) Raman spectrums of carbon samples.

Brunauer-Emmett-Teller (BET) adsorption-desorption plots (isotherms) of AC-PA/PP, AC-PA/PP/AP-0.25, AC-PA/PP/AP-0.5 and AC-PA/PP/AP-0.75 samples and their pore size distribution are presented in Fig. 2. The pore features of the obtained materials were further investigated by adsorption-desorption analyses. According to the IUPAC, all the isotherms in Fig. 2 (a) follow similar shapes which are typical type I adsorption-desorption with H4 hysteresis loop corresponding to the co-existence of well-developed micropores and mesopores [53].

The N_2 adsorbed volume, in the lower region of the relative pressure ($0 < P/P_0 < 0.1$), displayed a narrow knee. This monolayer adsorption indicates that micropores exist in abundance in the

samples. Thus, at P/P_0>0.4, the isotherms showed a conspicuous hysteresis loop, implying that the samples possess a certain amount of the mesopores [54]. The isotherms of the different samples have been added in the supporting information (Fig. S2) with an inset showing the hysteresis loops. It can be seen (in Table 1) that with increase of the AP amount, the specific surface area (SSA) and pore volume first intensify then reduce, with AC-PA/PP/AP-0.5 being the optimum sample. This behaviour could be attributed to the efficient amount of AP in the samples allowing the cross-linked polymers PA/PP to interact with the AP. The high SSA can provide an more electrode /electrolyte contact area for ions to adhere, subsequently leading to a higher electric double layer dominance [49]. In addition, the numerous pores of the as-prepared material provide a large number of a reachable electrochemical active sites along with the internal area for the ion diffusion and electrode/electrolyte interfacial contact [55]. Besides, the heteroatoms created more defects in the carbon material as the results of the observed SSA. The surface functionalities might create more active sites in the material promoting a good wettability and boost the pseudocapacitance performance. Through enhancing the wettability, the diffusion resistance between the electrolyte ions and the material is expected to reduce (i.e. quick charge transfer) [56]. The decrease of the SSA for the AC-PA/PP/AP-0.75 (2340 $m^2\ g^{-1}$) could be due to the saturation of AP in the sample. When the AP is used in excess in AC-PA/PP/AP-0.75, the SSA decreases owing to the corrosion of some pores and also it shows that a certain amount of PA/PP did not react with the AP [57].

The pore size distribution (using DFT method), plotted in Fig. 2 (b) confirms that the samples contain both micropores (<2 nm) and mesopores (2 – 50 nm). The high amount of micropore will enhance the charge storage capability and the mesopores serve as the channels for the electrolyte ions [58]. The micropores act as active sites and contribute to the specific capacitance. The narrower range of mesopore enables the fast transport of the ions which boost

the electrochemical performance [59]. The AC-PA/PP/AP-0.5 can be a promising electrode material for SC due to high SSA and pore volume.

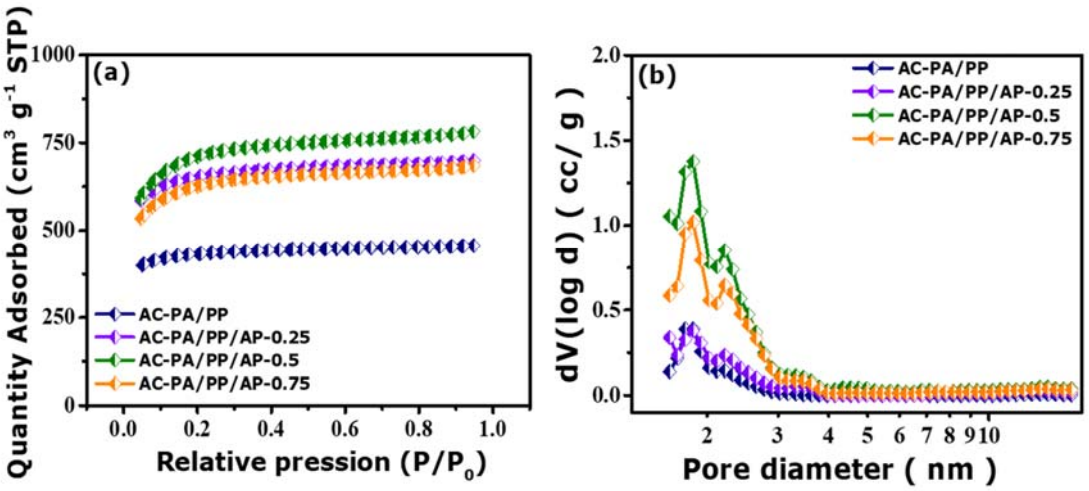

Fig. 2. (a) N_2 adsorption-desorption isotherms and (b) total pore size distribution plots of AC-PA/PP, AC-PA/PP/AP-0.25, AC-PA/PP/AP-0.5 and AC-PA/PP/AP-0.75 samples.

Table 1. Sample ID, SSA and pore volume

Sample ID	BET SSA (m^2 g^{-1})	Total pore volume (cm^3 g^{-1})
AC-PA/PP	1680	0.63
AC-PA/PP/AP-0.25	2480	0.96
AC-PA/PP/AP-0.50	2656	1.08
AC-PA/PP/AP-0.75	2340	0.94

The morphology of the produced porous carbons obtained using SEM characterization is shown in Fig. 3. It is visual that porous structure like morphology with an irregular

interconnected pore is exhibited in all samples. These results indicate that potassium hydroxide (KOH) play a significant role to produce pores in the carbon framework during activation at high temperature using the following eq. (1) [60][61]:

$$6KOH + 2C \rightarrow 2K + 3H_2 + 2K_2CO_3 \quad (1)$$

The decomposition of AP and KOH during the activation process leads to the formation of the functional groups such as quinone, carboxyl, phenolic [62][63]. The addition of AP (sources of N and P heteroatoms) induces irregularity in the carbon structure, which leads to more defects and active sites. AP does not only serve as N and P sources but also can act as activating agent to enhance the creation of pores in the carbon matrix. AP can enhance the penetration of KOH inside the carbon material and react with it. Production of the porous carbon is due to the synergistic effect of KOH and AP [64]. The decomposition of the diammonium hydrogen phosphate can be explained by the following Eqs. [65][66]:

$$(NH_4)_2HPO_4(s) \rightarrow NH_3(g) + NH_4H_2PO_4(s) \quad (2)$$

$$(NH_4)_2HPO_4(s) \rightarrow 2NH_3(g) + H_3PO_4(l) \quad (3)$$

$$NH_4H_2PO_4(s) \rightarrow NH_3(g) + H_3PO_4(l) \quad (4)$$

$$4H_3PO_4(l) \rightarrow 2H_2O(g) + 2H_4P_2O_7(l) \quad (5)$$

$$2H_4P_2O_7(l) \rightarrow H_2O(g) + P_4O_{10}(s) \quad (6)$$

The decomposition of $(NH_4)_2HPO_4$ lead to the phosphoric acid (H_3PO_4) and ammonia (NH_3) as seen in Eqs. (2) to (4) which arise at 159 °C and above. Phosphoric acid (H_3PO_4) and ammonia (NH_3) form instable amide by reacting with the carbon via the oxygen functional group to obtain N, P co-doping. Additionally, the reaction between H_3PO_4 and NH_3 with the carbon releases a large amount of gas such as H_2O, CO, within the material inducing a creation of more pores [67][68]. H_3PO_4 aid the pyrolysis to start, creates porosity in the sample and act as P source. NH_3 help on the formation of the pores and is an N source. Eqs. (5) and (6) take place from 209 °C and lead to the formation of the phosphorous pentoxide which sublimes at

579 °C. With the increase of AP amount, the porosity also changes as observed in Fig. 3 (e, f). AC-PA/PP/AP-0.5 possesses much rougher surface than others which suggest highly interconnected homogenously distributed pore structure.

Fig. S3 displays the energy-dispersive spectrometer (EDS) mapping of the as obtained carbon. It can be clearly seen that the samples contain uniformly distributed elements (C, O, N and P). The EDS shows that the AC-PA/PP was successfully doped as the samples shows N and P heteroatoms. As observed no any phosphorous was found in the AC-PVA/PVP. The nitrogen in this sample is due the presence of the PP.

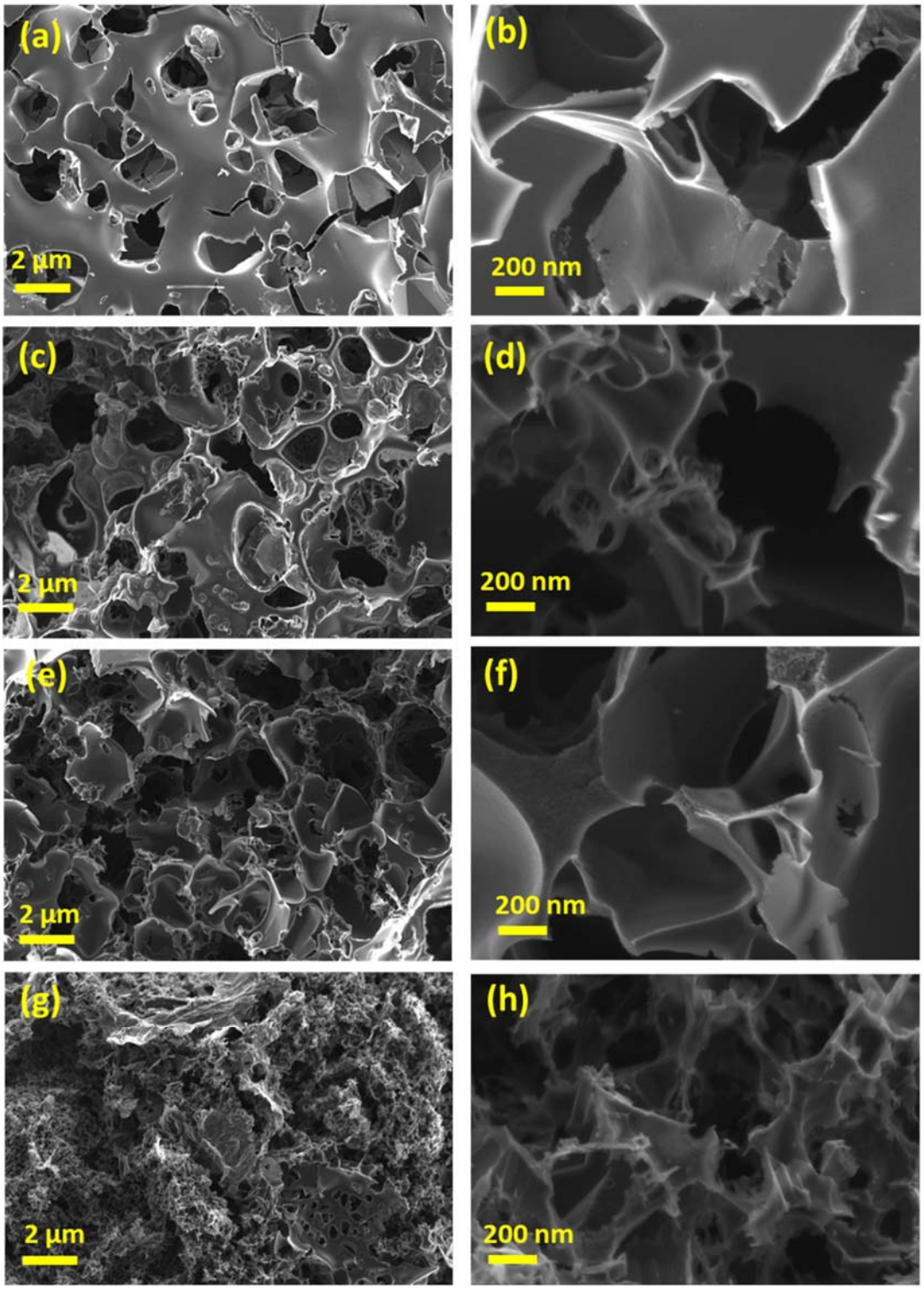

Fig. 3. SEM morphology at low and high magnification of (a-b) AC-PA/PP, (c-d) AC-PA/PP/AP-0.25, (e-f) AC-PA/PP/AP-0.5 and (g-h) AC-PA/PP/AP-0.75 samples, respectively.

Fig. 4 demonstrates the TEM micrographs of (a) AC-PA/PP, (b) AC-PA/PP/AP-0.25, (c) AC-PA/PP/AP-0.5 and (d) AC-PA/PP/AP-0.75 samples. These TEM images further confirm the presents of cavities as seen on the SEM morphology in Fig. 3. Moreover, the increase in AP content leads to the destruction of the irregular interconnected cavity framework resulting in a high concentrated narrow pore (rough morphology).

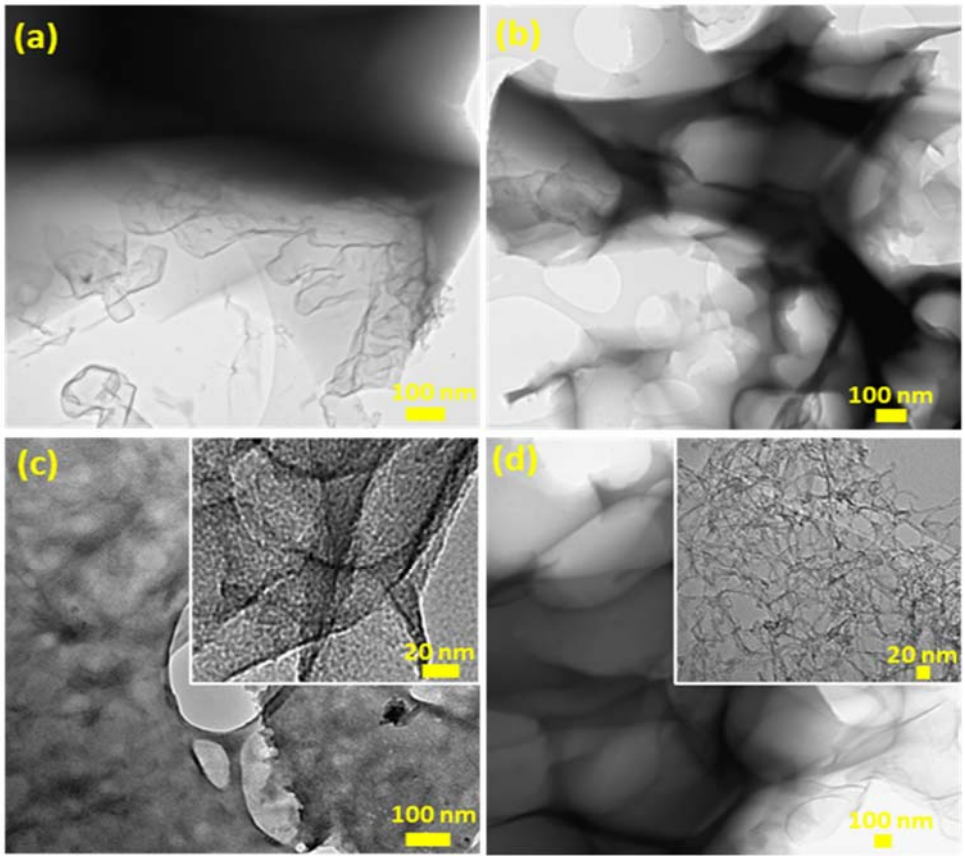

Fig. 4 TEM images of (a) AC-PA/PP, (b) AC-PA/PP/AP-0.25, (c) AC-PA/PP/AP-0.5 and (d) AC-PA/PP/AP-0.75 samples, and high magnification inset of AC-PA/PP/AP-0.5 and AC-PA/PP/AP-0.75

XPS measurement was carried out to gain an insight into the surface chemistry of AC-PA/PP and doped AC-PA/PP/AP-x sample as displayed on Fig. 5 (a). The figure depicted the XPS

survey spectra displaying four characteristics peaks around 284.6, 534, 400 and 134.8 eV which can be allotted to C1s, O1s, N1s and P2p, respectively [69] while the pristine lacks phosphorus as seen on EDS results. Even with a low amount of N and P in the sample, the XPS survey show peaks with very low intensity. Some studies have reported a small amount of N and P which were displayed on the survey and deconvoluted at high resolution [70][71][64][67] The atomic percentage of each element determined by integrating areal peaks of the XPS data (see Fig. 5 (b) and Fig. S4, S5, S6, S7). It can be observed that as AP increases, nitrogen content increases from 0.84 % for AC-PA/PP/AP-0.25 to 1.25 % for AC-PA/PP/AP-0.5 then decrease to 1.00 % for AC-PA/PP/AP-0.75. A similar trend is observed for the phosphorous content as seen in Table S2. This suggests that dopant content depends on the amount of AP. Furthermore, phosphorous-doping has a significant impact in the concentration of oxygen functionalities (surface oxygen content) [37]. The AC-PA/PP/AP-0.5 has the highest N, P and O content due to the appropriate AP-doing content which has led to more creation of more active sites. This is in line with the Raman results in terms of I_D/I_G ratio suggesting more defect attributed to accommodation of high amounts of N, P within the carbon matrix. The highest percentage of phosphorous and nitrogen in AC-PA/PP/AP-0.5 sample might increase the specific capacitance through significant redox reaction, increased conductivity and also the high possible wettability due to different nitrogen formations. AC-PA/PP/AP-0.5 displays the lowest carbon content. More carbon atoms are likely lost as CO and CO_2 when nitrogen is integrated into the carbon matrix [57][67]. AC-PA/PP/AP-0.75 display the highest carbon content. This can be explained by the fact that more carbon atoms did not get replaced by the nitrogen and phosphorous. Saturation was obtained with the addition of an excess of AP leading to a non-synergistic effect of AP and carbon.

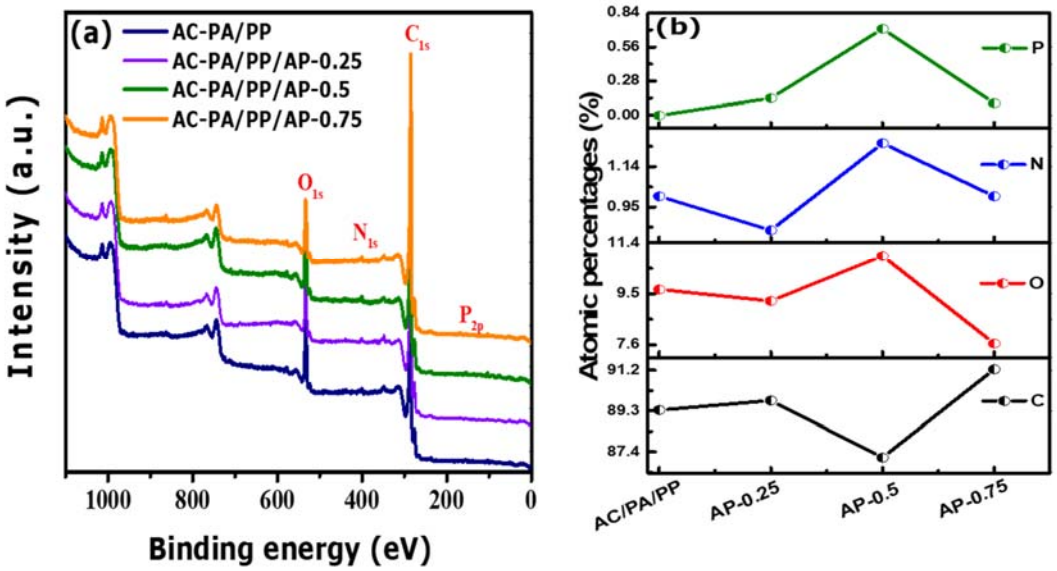

Fig. 5. (a) XPS survey spectra and (b) atomic percentage of AC-PA/PP, AC-PA/PP/AP-0.25, AC-PA/PP/AP-0.5 and AC-PA/PP/AP-0.75 samples.

To evaluate the surface chemical state for each sample, high resolution XPS spectra of C1s, O1s, N1s and P2p were further analysed. The deconvolution of different elemental peaks for the AC-PA/PP/AP-0.5 is illustrated in Fig. 6, while those of other samples are displayed in Fig. S8-S10. The C1s XPS peak in Fig. 6 (a) can be deconvoluted into four distinct peaks at 284.49, 285.22, 287.26 and 289.98 eV attributed to C-C, C-N/C-P, C-O and COO, respectively [49][72][73]. The C-N/C-P deconvoluted peak presence the bonding of C-N and/or C-P which indicates that some carbon atoms were substituted by nitrogen and phosphorous [73]. Fig. 6 (b) displays three high resolution deconvoluted peaks located at 531.03, 533.02 and 535.47 eV of the for the O1s which can be assigned to C=O/P=O, (O-I), C-O/C-OH(O-II), COOH (O-III) and/or water group, respectively [74][75]. Note that, high oxygen functional groups amount can contribute in the wettability and also increase pseudocapacitance behaviour due to the O-I and O-II which provide electrochemical active sites [53][76][77][78].

The high resolution of N1s spectrum displayed in Fig. 6 (c) was deconvoluted into four characteristic peaks at binding energies of 398.74, 399.98, 400.81 and 402.26 eV related to pyridinic N, pyrrolic N, graphitized N and nitrogen oxide, respectively [73][79]. The nitrogen-containing functional groups, such as, graphitized N peak which can be related to the P-N bonding, pyridinic N and pyrrolic N played a key role in SC application by enhancing the capacitive charge storage [79][80]. By introducing lone pair electrons in π system, Pyridinic N can generate electrochemical active sites and induce pseudocapacitance. Pyrrolic N has a good electron donor property and displays excellent charge mobility. Pyridinic and pyrrolic can enhance the pseudocapacitance through redox reaction. They create defects and increase the number of active sites. Redox reactions can involve nitrogen in pyridinic and pyrrolic which are highly active sites and act as additional defects for ions adsorption [81][82]. Graphitized N enhance the electrical conductivity, which effectively minimizes the electron transfer resistance, and further improves the performance [9][49]. Graphitic and pyridinic-N-oxides are significant for increasing capacitance by facilitating electron transport, when distributed in the pores that are accessible to the ions [83]. The introduction of the lone pair of electrons by the N dopant, decrease the band gap by relocating the Fermi level into the conduction band. With electrolytic ions, the active sites have more incredible binding energy leading to the accommodation of tremendous number of ions on the surface of the electrode material [84]. AC-PA/PP/AP-0.5 has the highest percentage of pyridinic N and nitrogen oxide suggesting the highest transport rate of electron and an improvement of electrochemical performance [79][80]. N-doping can boost the wettability of electrode/electrolyte interface by providing additional pseudocapacitance [75]. After the introduction of diammonium hydrogen phosphate, the content of nitrogen in AC-PA/PP/AP-0.5 increases from 1.0 to 1.25 suggesting that the dopant precursor played a significant role in enhancing the amounts of N species. Dual doping is

advantageous for additional active sites and edge defects. In this study, the co-doping of P and N resulted in no meaningful increase on the surface concentration of N.

However, the spectrum of the P2p in Fig. 6 (d) contains two peaks with overlapped doublet arising owing to 2P3/2 and 2P1/2 spin states at 134.4 ± 0.5 eV and 135.3 ± 0.5 eV. The former attributed to P-C and the latter P-O [85][86][87]. The existence of P-O bonding suggested that the doped P atoms in the pyrolysis process could be partially oxidized [37]. The presence of phosphorous-oxygen bonding (redox active) could be a significant influencing factor on oxygen content and can provide electroactive sites. Phosphorous was expected to have higher oxygen affinity than nitrogen. The P-C bond might indeed play a significant role to enhance the electronic conductivity. This is advantageous in improving the capacitance performance [88]. Porous carbon has various oxygen functionalities. Not all surface oxygen function, nevertheless, are stable; the deterioration of the capacitance during cycling is linked to these unstable surface oxygen groups (O-III or HO-C=O). Phosphorous incorporation into the carbon can suppress the production of these unstable groups by forming a protective oxide layer on the surface of the carbon sample [74]. Phosphorous has a higher radius than carbon because of that its incorporation does not happen in the graphitic lattice. Phosphorous displays sp^3configuration and contribute to provide more active sites [83]. AC-PA/PP/AP-0.5 sample have higher P content (0.71%) than AC-PA/PP/AP-0.25 (0.14%) and AC-PA/PP/AP-0.75 (0.10%). This indicates that the amount of diammonium hydrogen phosphate have a major influence on the P species percentage. The phosphorous lone pair electron might provoke electrochemical activity in the carbon framework [40].

The carbon material co-doped with N, P can promote the morphology, hydrophilicity, stability, specific capacitance of the recovered material while also boosting its electrochemical performance owing to the presence of various functionalities at the surface [49][89].

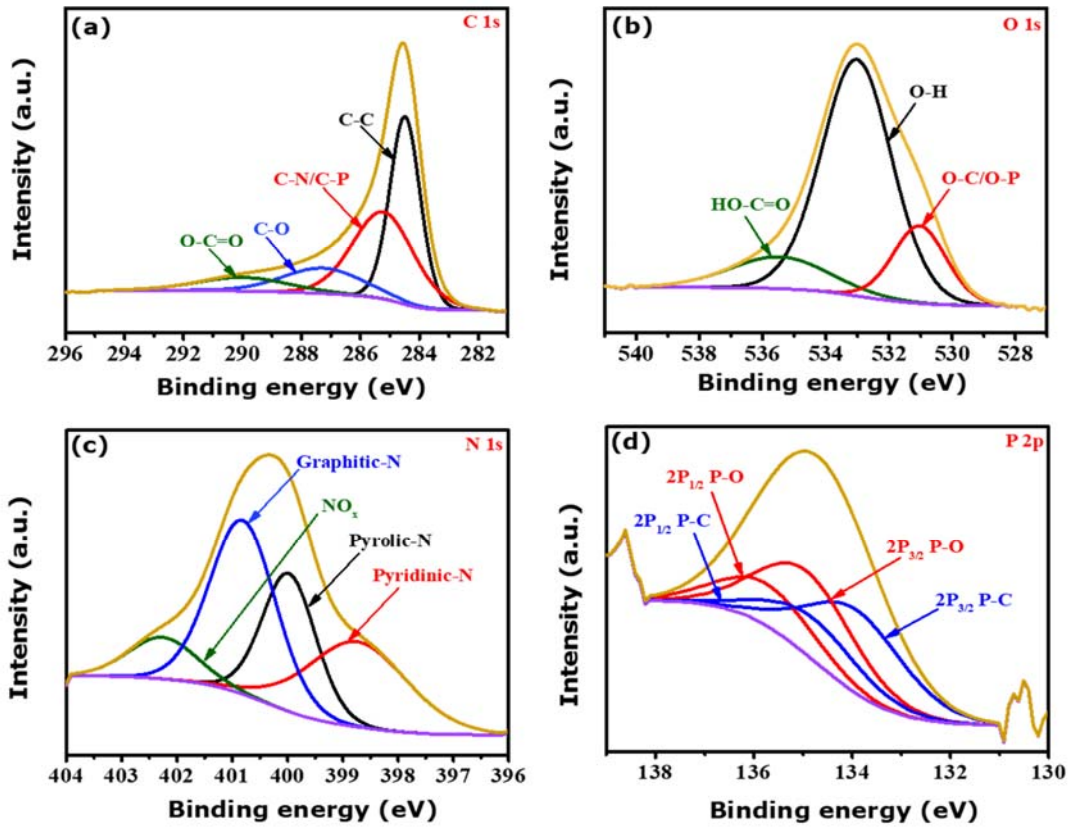

Fig. 6. XPS spectra deconvoluted (a) C1s, (b) O1s, (c) N1s and (d) P2p of the as-synthesized AC-PA/PP/AP-0.5 sample.

3.2 Electrochemical performance

3.2.1. Three-electrode evaluations

To investigate the electrochemical behaviour of AC-PA/PP, AC-PA/PP/AP-0.25, AC-PA/PP/AP-0.5 and AC-PA/PP/AP-0.75 were measured in three electrode set-up using 2.5 M KNO_3 aqueous electrolyte. The CV curves of the sample in positive and negative potential windows are displayed in Fig. 7 (a) and (b) and were measured at a scan rate of 50 mV s^{-1}. The samples exhibited a rectangular shape without the presence of redox peaks, strongly suggesting EDLC behaviour. Among them, AC-PA/PP/AP-0.5 has the best current response i.e., largest

CV area which implies the highest specific capacitance. This behaviour could be due to the improved porosity, high SSA, surface reactivity and adequate dopant amount (N, P). These are beneficial for charge storage and ions transport at the electrode/electrolyte interface. Moreover, surface functionalization due to the heteroatoms has enhanced the hydrophilicity of the carbon electrode, leading to improving its electrochemical performance [9]. A comparative CV of Ni foam and the AC-PA/PP is given (Fig. S11) to show that the influence of Ni foam on the electrochemical performance of the samples is negligeable in 2.5 M KNO_3. GCD curves measured at 1 A g^{-1} is shown in Fig. 7 (c) and (d) displays a slightly distorted triangular shape, demonstrating capacitive behaviour and the reversibility of the materials with the contribution of additional pseudocapacitance (presence of heteroatoms) [40][35]. The GCD of the AC-PA/PP/AP-0.5 has a greater discharge time amongst other samples due to high nitrogen and phosphorous content as indicated by the XPS results.

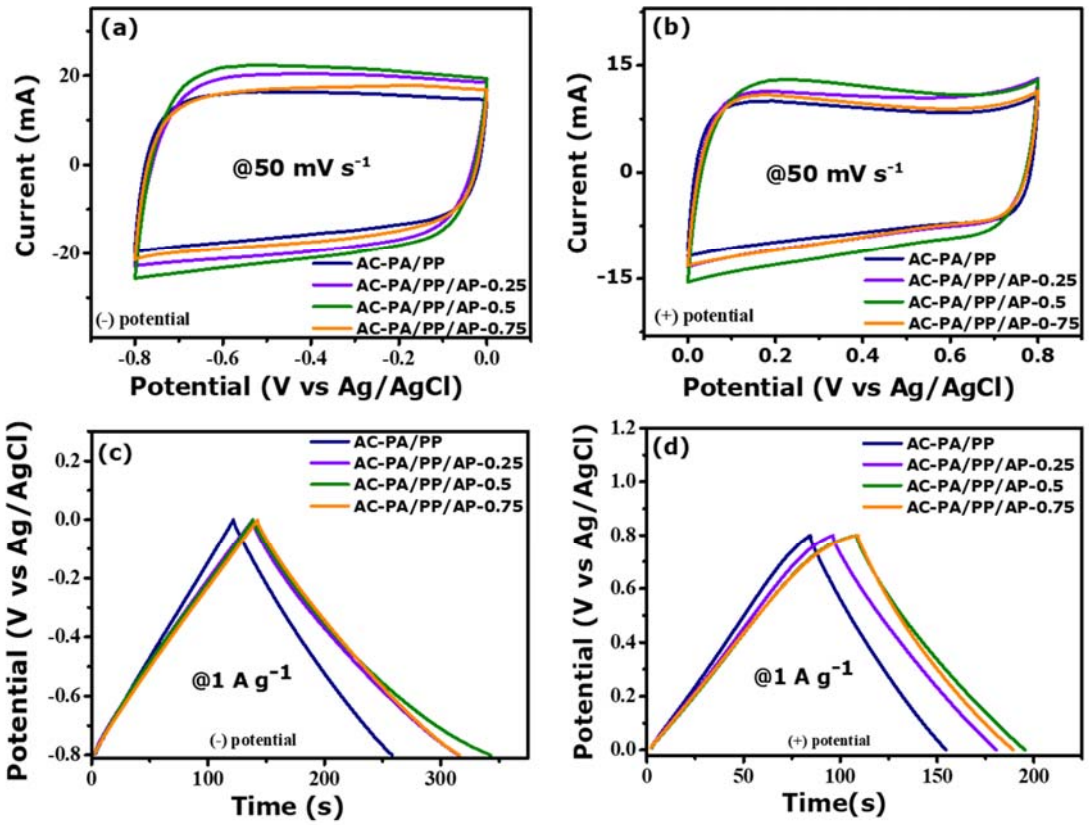

Fig. 7. (a-b) CV and (c-d) GCD plots of AC-PA/PP, AC-PA/PP/AP-0.25, AC-PA/PP/AP-0.5 and AC-PA/PP/AP-0.75 samples.

Further GCD evaluations were performed to understand the specific capacitance at various specific currents (Fig. 8 (a) and (b)). The specific capacitance was calculated using Eq. (S1) for both GCD in negative and positive potentials. The specific capacitance of 170, 222, 252 and 220 F g^{-1} were recorded for AC-PA/PP, AC-PA/PP/AP-0.25 AC-PA/PP/AP-0.5 and AC-PA/PP/AP-0.75, respectively at 1 A g^{-1} in the negative potential window. AC-PA/PP/AP-0.5 showed higher specific capacitance than AC-PA/PP, AC-PA/PP/AP-0.25 and AC-PA/PP/AP-0.75 for all specific currents reported which was assigned to its highly porous network

structure, presence and appropriate heteroatom doping amount and high specific surface area. The better performance of the AC-PA/PP/AP-0.5 can be further be attributed to the highest phosphorus content compared to the other samples [90]. On the other hand, the AC-PA/PP/AP-0.5 was noted to outperform other heteroatom doped carbon samples on the positive potential window as shown in Fig. 8 (b). Furthermore, AC-PA/PP/AP-0.5 still demonstrated a good specific capacitance of 82 F g^{-1} and 174 F g^{-1} and in both positive and negative potential at a higher specific current of 10 A g^{-1} indicating a good capacitance retention of 69% and 75%, respectively. It is worth noting that the synergistic effect of potassium hydroxide, and ammonium phosphate dibasic, have a significant effect on the electrochemical performance of the as-prepared AC-PA/PP/AP-0.5 sample. Also, the micropores and mesopores in this particular sample are suitable to accommodate the electrolyte ions. AC-PA/PP/AP-0.75 recorded the lowest specific capacitance than other co-doped materials owing to the high dopant concentration and incomplete activation.

Fig. 8 (c) described the Nyquist plots with an inset regarding all samples, investigating the transport characteristics of the charge carriers and the internal resistance. At low frequency, all curves showed a quasi-vertical shape of capacitive behaviour with faster ion transport and low diffusion resistance of the ions within the carbon material. As observed, all materials exhibited similar inconspicuous arcs in high frequency indicating the interfacial charge transfer resistance (R_{CT}) and mass transport. The intercepts of the real x-axis of the semi-circle shows the equivalent series resistances (ESR). ESR represents the contact resistance at the active material/current collector and the internal resistance of the electrode/electrolyte [49]. The ESR was found to be 1.8; 1.3; 1.2 and 1.6 Ω for AC-PA/PP, AC-PA/PP/AP-0.25, AC-PA/PP/AP-0.5, AC-PA/PP/AP-0.75 samples, respectively. Clearly, better performance is still established by AC-PA/PP/AP-0.5 whereby it presents the shortest diffusion length, the smallest ESR and is closer to the y-axis as compared to others. These results suggest that, due to the doping, AC-

PA/PP/AP-0.5 has a good interaction between electrode material and the electrolyte/or current collector, a faster ion diffusion in the electrolyte and a good electrical conductivity [78]. The high specific surface area (2640 $m^2 g^{-1}$) involves an enlarged contact area between the electrode and the electrolyte which suggest more active site for charge storage. The low ESR of the AC-PA/PP/AP-0.5 is in agreement with the high specific surface area, the well-developed porous carbon (beneficial for electrolyte ions migration to the electrode surface) and the high specific capacitance. The wettability was enhanced owing to the presence and the right amount of nitrogen and phosphorous at the surface of the electrode material [35][78]. Thus, AC-PA/PP/AP-0.5 is regarded as a new promising electrode material in SCs applications with high electrochemical properties.

The electrochemical performances of the AC-PA/PP/AP-0.5 at different scan rates and specific current in 2.5 M KNO_3 electrolyte are plotted in Fig. S12 (supporting information). The CV curves on Fig. S12 (a) and (b) displayed rectangular shape at different sweeping rates increasing from 10 to 100 mV s^{-1} in both negative and positive potential. GCD curves shown in Fig. S12 (c) and (d) exhibit triangular shape at the sweep rates from 1 to 10 A g^{-1} confirming the capacitive behaviour and the good rate capability of the sample as observed in Fig. S12 (a) and (b). Fig. S13 in the supporting information shows the GCD cycling stability of the as-prepared samples electrodes conducted at a specific current of 5 A g^{-1} for up to 5000 cycles. From the Fig. S13 (c), AC-PA/PP/AP-0.5 electrode showed a better stability in terms of both capacitance retention of 99.8% and coulombic efficiency (100%) as compared to AC-PA/PP, AC-PA/PP/AP-0.25 and AC-PA/PP/AP-0.75 electrodes.

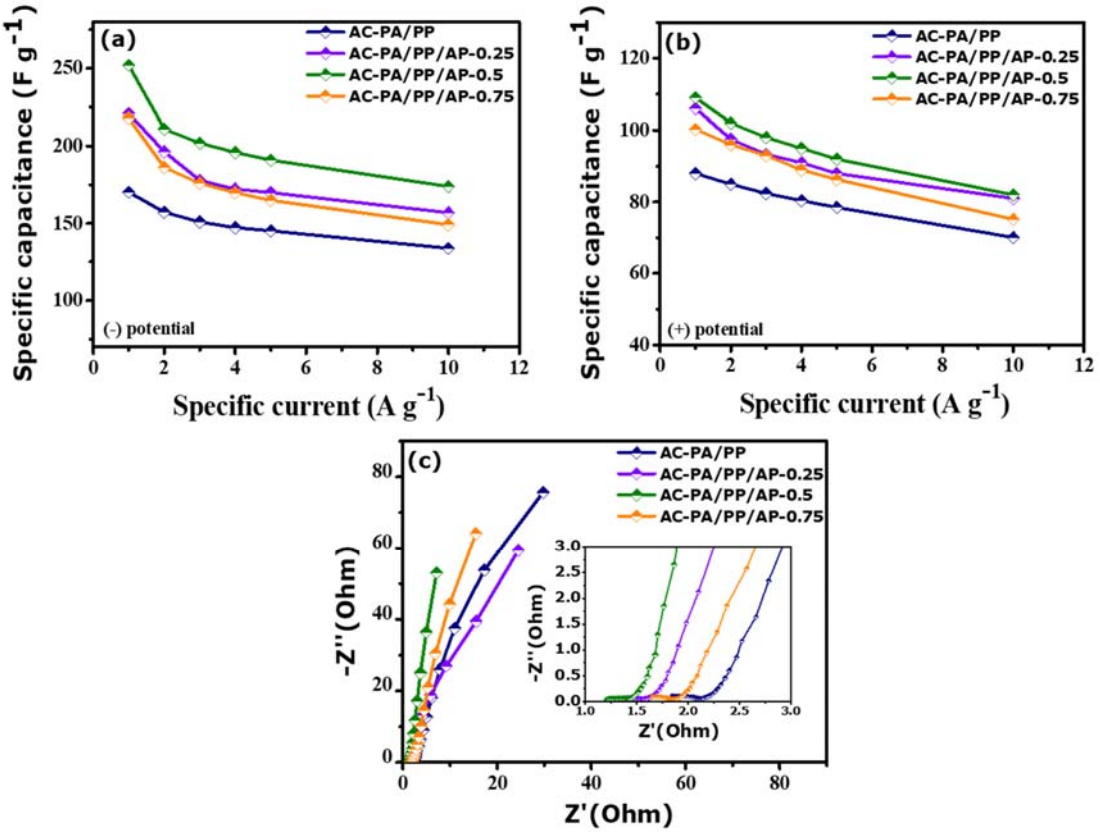

Fig. 8. (a-b) specific capacitance versus specific current and (c) EIS Nyquist plots of AC-PA/PP, AC-PA/PP/AP-0.25, AC-PA/PP/AP-0.5 and AC-PA/PP/AP-0.75 samples, respectively.

3.2.2. Two-electrode evaluations

A two-electrode test was conducted to further quantify the electrochemical performance and demonstrate the applicability of AC-PA/PP/AP-0.5 electrode in practical SC applications. A symmetric SC AC-PA/PP/AP-0.5//AC-PA/PP/AP-0.5 was assembled by two identical AC-PA/PP/AP-0.5 electrodes material using a split cell test with the same 2.5 M KNO_3 electrolyte. Fig. 9 (a) shows the CV features of the fabricated device at various scan rate ranging from 10 to 100 mV s^{-1} within a maximum achievable operating cell potential of 1.6 V. The CV curves

display a quasi-rectangular shape revealing the perfect capacitance nature of the device and implying that the electron transport kinetics are quasi reversible [91][92]. Even at high scan rate of 100 mV s^{-1} the CV curves still maintain a well retained shapes, revealing the excellent rate capability of the CD process and better implication of surface area and pores of the as-synthesized carbon material for charge storage [84]. For comparison, the CV of a device using only Ni foam and the optimized sample are displayed in Fig. S14 to show that the Ni foam doesn't not interfere on the performance on the electrode material.

Fig. 9 (b) displayed the galvanostatic CD plots of the fabricated device at different specific currents (0.5 to 10 A g^{-1}) in the identical operating potential. The GCD exhibited a triangular shape representing a good EDLC material. The slight deviation is due to the presence of the heteroatom's functionalities [93]. Fig. 9 (c) showed the specific capacitance values of the assembled cell as a function of the specific current from 0.5 to 10 A g^{-1}. The calculated specific capacitance of the as-assembled AC-PA/PP/AP-0.5//AC-PA/PP/AP-0.5 SC using Eq. (1), presented a maximum value of 76.9 F g^{-1} at 0.5 A g^{-1}. Furthermore, as the specific current increase, the specific capacitance decreases as well. This phenomenon is due to the limited reaction and ions transfer at the electrode's surface at high specific current [94]. Even at high specific current of 10 A g^{-1}, the symmetric cell still recorded a high specific capacitance of 61.4 F g^{-1} demonstrating the impressive rate capability of 79.8 %. Fig. 9 (d) displayed the Ragone plot of the symmetric SC device with specific energy of 27.3 W h kg^{-1} and a specific power of 400 W kg^{-1} measured at 0.5 A g^{-1}. The Ragone plots further illustrates the higher specific energy and specific power of the fabricated symmetric device in comparison to other devices for SC applications produced using nitrogen/phosphorous co-doped porous carbon from the literature [41][43][69][72][95][96]. Moreover, even at high specific current of 10 A g^{-1}, the specific energy remained at 21.8 W h kg^{-1} with a specific power of 8.0 kW kg^{-1}. Furthermore, a comparative study for symmetric devices is presented in Table 2. It is notable that AC-

PA/PP/AP-0.5 electrode was achieved a higher capacitance and rate efficiency compared to the existing doped porous carbon electrode material, which is attributed to the cross-linking architecture of AC-PA/PP/AP-0.5 to facilitate charge transfer and high SSA to offer more active sites for the accommodation of electrolytes ions.

Table 2: Comparison of the electrochemical performance of multi-doped porous carbon derived from various precursors for symmetric devices.

Precursors	Electrolyte	I_d (A g^{-1})	E_d (Wh kg^{-1})	P_d (W kg^{-1})	Ref
Lignin/Chitosan	EMIM TFSI[a]	0.5	11.5	4500	[97]
Polyacrylonitrile	PVA/KOH[b]	0.1	21.31	500	[98]
Onion Skin	1M Na_2SO_4[c]	1	17	150.6	[99]
PVDF	6 M KOH[d]	0.5	23.1	702.4	[100]
Rapeseed cake	1 M Na_2SO_4[c]	0.05	21	50	[101]
PPy/PT	6 M KOH[d]	0.2	16.2	50	[102]
PA/PP	2.5 M KNO_3[c]	0.5	27.2	400	This work

I_d ~ specific current, E_d ~ specific energy, P_d ~ specific power, PVDF~ Polyvinylidene fluoride, PPy ~ Polypyrrole, PT ~ Polythiophene, *a* ~ ionic liquid electrolyte, *b* ~ gel electrolyte, *c* ~ neutral aqueous electrolyte, and *d* ~ basic aqueous electrolyte.

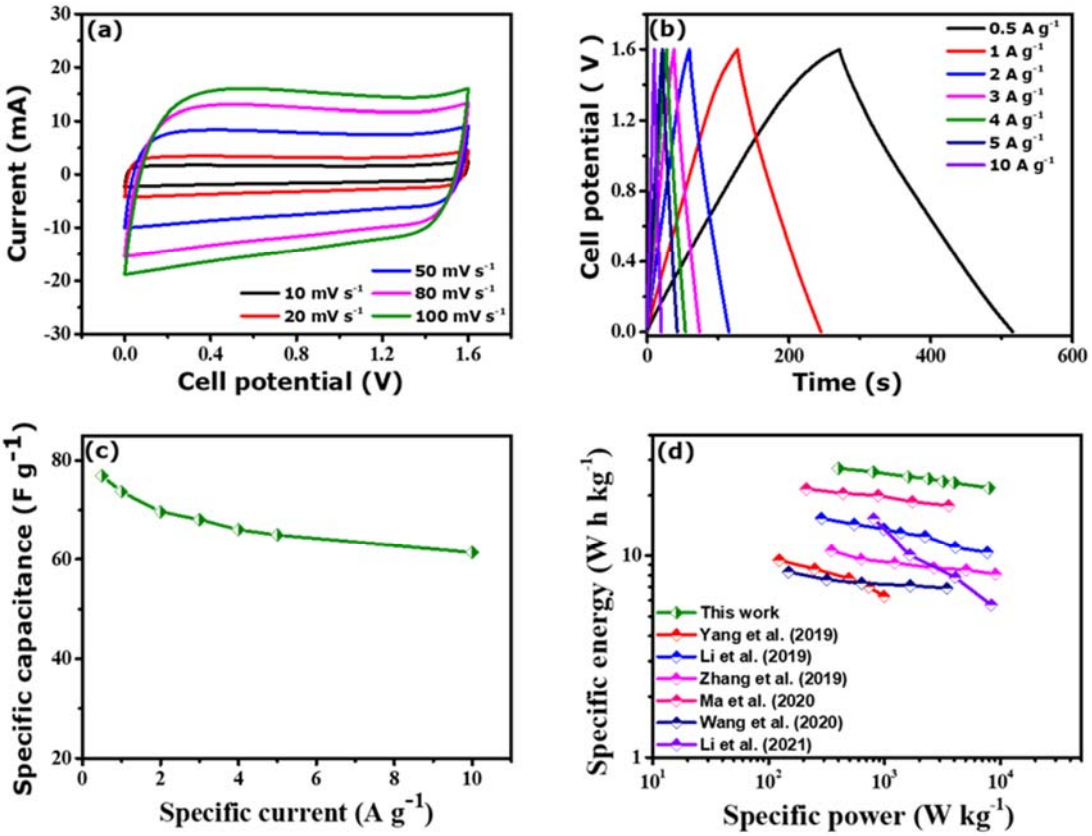

Fig. 9. (a) CV at various scan rates, (b) GCD at various specific currents, (c) specific capacitance as a function of specific currents and (d) Ragone plot of the AC-PA/PP/AP-0.5//AC-PA/PP/AP-0.5 SC.

The long-term cyclic stability of the fabricated AC-PA/PP/AP-0.5//AC-PA/PP/AP-0.5 cell, is an important factor for its practical applicability. The cyclic stability of the constructed symmetric device was performed by continuous CD measurements at 5 A g^{-1} up to 10,000 cycles (Fig. 10 (a)). The SC exhibited 90 % capacitance retention and a good coulombic efficiency of 99.8 % at a constant CD cycle.

Fig. 10 (b) showed the floating test (voltage holding) upon five days (120 h) at 5 A g^{-1} at a maximum potential of 1.6 V. For the first 20 h, the specific capacitance of the device declines.

Between 20 h to 40 h, the increase of the specific capacitance is noted before stabilizing after 50 h. The improvement of the specific capacitance might be attributed to the great accessibility of electrolyte's ions into the pores of carbon matrix, during the repeated floating test, enhancing the wettability and the ions diffusion at the electrode/electrolyte interface [91]. As seen in the previous work done by Fasakin et al. [103] with a prolonged device operation at high operating potentials, the activated carbon is expanded and the previously quiescent pores are exposed, resulting in an enhanced capacitance. Indeed, this can increase the charge storage of the symmetric device demonstrating the good stability of the device.

The GCD curves, at 5 A g^{-1} before and after 10,000 cycling stability as well as after voltage holding are plotted in Fig. 10 (c). The discharge time in the galvanostatic charge/discharge plots slightly decreased after the device being subjected to 10,000 cycles. The shape was maintained proving the good stability of the device. The contrived SC displayed a longer discharge time after floating time suggesting a better capacitance owing to the fast transfer rate at electrode/electrolyte interface. The obtained Nyquist plots of the as-fabricated AC-PA/PP/AP-0.5//AC-PA/PP/AP-0.5 cell, before and after 10,000 cycling stability and also floating time, are shown in Fig. 10 (d). As seen in the inset to the figure, all the curves revealed a quasi-vertical line at low frequency indicating a capacitive behaviour of the symmetric SC. The device's solution resistance (R_s) or equivalent solution resistance (ESR) is the overall sum of resistances including the ionic resistance of electrolyte, intrinsic resistance of the active materials and contact resistance at the interface between the active electrode material and current collector. The R_s value increased from 0.61 Ω before cycling to 0.71 Ω after the stability test, then decrease to 0.60 Ω after the voltage holding test probably due to the change in of the intrinsic resistance of the active material (see the inset to Fig. 10 (d)). The minor semicircle diameter demonstrated a decrease of the charge transfer resistance (R_{CT}), high ions electrolyte diffusion and a better electrical conductivity. The introduction of the phosphorous is

responsible for the improved wettability implying the smallest ESR and the R_{CT} [84]. After long term cyclic stability and floating test, AC-PA/PP/AP-0.5//AC-PA/PP/AP-0.5 constructed symmetric SC, exhibited an improved surface wettability, enhanced conductivity, and a better ion diffusion. Due to the synergistic effect of AP and KOH leading to the high SSA, the dual doping contribution inducing the pseudocapacitance (sufficient actives sites), the AC-PA/PP/AP-0.5//AC-PA/PP/AP-0.5 can be a potential candidate for energy storage device. The EIS fitting of the plots displayed in Fig. 10 (e) by using equivalent circuit diagram in the inset to this were generated via the ZFIT/EC-Lab version 11.33 using the Randomise + Simplex method. The fitting was obtained at the optimized minimization error i.e. chi-squared ($\chi 2$) and $\chi/\sqrt{N}$. The $\chi/\sqrt{N}$ is a normalized expression of $\chi 2$, where N is the number of data points, whose value is independent of the number of points. It can be seen from the Nyquist plot on Fig. 10 (d) that the is an insignificant difference between the three EIS spectra. Thus, one equivalent circuit fitted all the EIS spectra. In the equivalent circuit, the R_s is connected in series with a constant phase element Q, which is connected in parallel with the R_{CT} and Warburg diffusion element (W). The W which is responsible for transition from high to low frequency is connected in series with R_{CT}. Ideally, at very low frequencies, an ideal polarizable capacitive electrode with the mass capacitance (C) should give rise to a straight line parallel to the imaginary axis. However, from the Nyquist plot in Fig. 10 (d) there is a divergence from this ideal capacitor behavior. This divergence is attributed to the existence of a leakage current resistance (R_L) which is in parallel to C. Table 3 summarizes all the EIS fitting parameters.

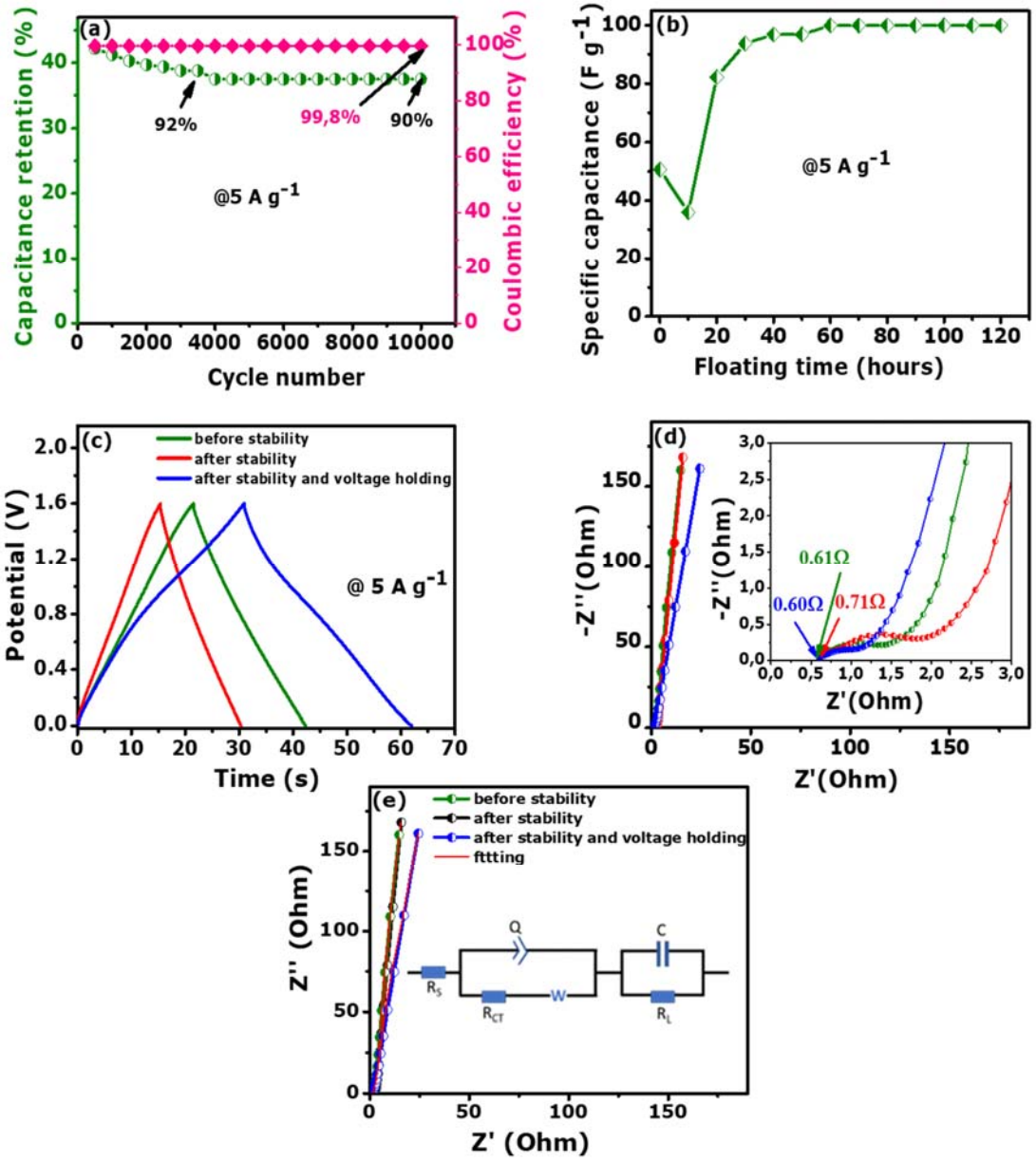

Fig. 10. (a) Capacitance retention and columbic efficiency against cycle number, (b) specific capacitance versus voltage holding time up to 120 h, (c) GCD curves, (d) Nyquist plot and (e) EIS fitting equivalent circuit of device before and after voltage holding for the AC-PA/PP/AP-0.5//AC-PA/PP/AP-0.5 symmetric SC.

Table 3. Sample ID and EIS numerical fitting parameters

Sample ID	R_s (Ω)	Q ($Fs^{(a-1)}$)	a	R_{CT} (Ω)	A_W ($\Omega s^{-1/2}$)	C_L (F)	R_L (KΩ)
Before stability	0.5071	0.01697	0.4427	1.249	1.693	0.1045	3.345
After stability	0.6154	0.0102	0.4825	1.6420	2.086	0.09938	4.988
After stability and voltage holding	0.576	0.01339	0.5253	0.6104	2.464	0.1057	1.523

4. Conclusion

In summary, in this study we presented a simple and practical one-step activation synthesis approach for producing nitrogen/phosphorous co-doped activated carbon material from cross-linked polymers (polyvinyl alcohol and polyvinyl pyrrolidone) with good electrochemical performance. This is due to the co-doping specifically phosphorous doping which enhances the pseudocapacitance performance and the wettability of the electrode material. The cross-linking creates a highly interconnected porous framework with micropores and mesopores. The high specific surface area and the great porous structure originated from the synergistic effect of the ammonium hydrogen phosphate and potassium hydroxide. These features yield more active sites, stored charges, and aid to the fast diffusion of electrolytes ions into the porous carbon electrode. The optimal AC-PA/PP/AP-0.5 displayed the highest specific surface area of 2656 $m^2\ g^{-1}$ and a specific capacitance of $252\ F\ g^{-1}$ at $1\ A\ g^{-1}$. The fabricated symmetric SC AC-PA/PP/AP-0.5//AC-PA/PP/AP-0.5 delivered a great specific energy and power of 27.3 W h kg^{-1} and 400 W kg^{-1}, respectively at a specific current of 0.5 A g^{-1}. A good stability and capacitance retention of 99.8% and 90% up to 10,000 cycles respectively was noted for the symmetric device. The device further indicated an excellent floating test (voltage holding) for up to 120 h at 5 A g^{-1}. Therefore, the outcome of this work confirmed that AC-PA/PP/AP-0.5 has a great potential for practical SC applications.

Acknowledgement

This study is sustained by the South African Research Chairs Initiative in carbon Technology and Materials of the Department of Science and Technology and National Research Foundation (NRF) of South Africa (Grant No. 61056). The observations, opinions, and conclusion specified in this work are those of the author(s), and the NRF does not take any liability in this regard. D. T. Bakhoum acknowledges the financial support from the Organization for Women in Science for the Developing World (OWSD) and Swedish International Development Cooperation Agency (Sida) and the University of Pretoria.

References

[1] S. Liu, K. Chen, Q. Wu, Y. Gao, C. Xue, X. Dong, Ulothrix-Derived Sulfur-Doped Porous Carbon for High-Performance Symmetric Supercapacitors, ACS Omega. 7 (2022) 10137–10143. https://doi.org/10.1021/acsomega.1c06253.

[2] M. Peng, L. Wang, L. Li, Z. Peng, X. Tang, T. Hu, K. Yuan, Y. Chen, Molecular crowding agents engineered to make bioinspired electrolytes for high-voltage aqueous supercapacitors, EScience. 1 (2021) 83–90. https://doi.org/10.1016/j.esci.2021.09.004.

[3] D.J. Tarimo, K.O. Oyedotun, N.F. Sylla, A.A. Mirghni, N.M. Ndiaye, N. Manyala, Waste chicken bone-derived porous carbon materials as high performance electrode for supercapacitor applications, J Energy Storage. 51 (2022) 104378. https://doi.org/10.1016/j.est.2022.104378.

[4] S. He, G. Chen, H. Xiao, G. Shi, C. Ruan, Y. Ma, H. Dai, B. Yuan, X. Chen, X. Yang, Facile preparation of N-doped activated carbon produced from rice husk for CO2 capture, J Colloid Interface Sci. 582 (2021) 90–101. https://doi.org/10.1016/j.jcis.2020.08.021.

[5] S. Sarr, N.F. Sylla, D.T. Bakhoum, K.O. Oyedotun, B.D. Ngom, N. Manyala, Effect of neutral electrolytes on vanadium dioxide microspheres-based electrode materials for asymmetric supercapacitors, J Energy Storage. 43 (2021) 103294. https://doi.org/10.1016/j.est.2021.103294.

[6] D.J. Tarimo, K.O. Oyedotun, A.A. Mirghni, N.F. Sylla, N. Manyala, High energy and excellent stability asymmetric supercapacitor derived from sulphur-reduced graphene oxide/manganese dioxide composite and activated carbon from peanut shell, Electrochim Acta. 353 (2020) 136498. https://doi.org/10.1016/j.electacta.2020.136498.

[7] B.D. Ngom, N.M. Ndiaye, N.F. Sylla, B.K. Mutuma, N. Manyala, Sustainable development of vanadium pentoxide carbon composites derived from Hibiscus

sabdariffa family for application in supercapacitors, Sustain Energy Fuels. 4 (2020) 4814–4830. https://doi.org/10.1039/d0se00779j.

[8] R. Zhang, W. Zhang, M. Shi, H. Li, L. Ma, H. Niu, Morphology controllable synthesis of heteroatoms-doped carbon materials for high-performance flexible supercapacitor, Dyes and Pigments. 199 (2022) 109968. https://doi.org/10.1016/j.dyepig.2021.109968.

[9] N.F. Sylla, N.M. Ndiaye, B.D. Ngom, B.K. Mutuma, D. Momodu, M. Chaker, N. Manyala, Ex-situ nitrogen-doped porous carbons as electrode materials for high performance supercapacitor, J Colloid Interface Sci. 569 (2020) 332–345. https://doi.org/10.1016/j.jcis.2020.02.061.

[10] N.M. Ndiaye, N.F. Sylla, B.D. Ngom, F. Barzegar, D. Momodu, N. Manyala, High-performance asymmetric supercapacitor based on vanadium dioxide/activated expanded graphite composite and carbon-vanadium oxynitride nanostructures, Electrochim Acta. 316 (2019) 19–32. https://doi.org/10.1016/j.electacta.2019.05.103.

[11] M. Vinayagam, R. Suresh Babu, A. Sivasamy, A.L. Ferreira de Barros, Biomass-derived porous activated carbon from Syzygium cumini fruit shells and Chrysopogon zizanioides roots for high-energy density symmetric supercapacitors, Biomass Bioenergy. 143 (2020) 105838. https://doi.org/10.1016/j.biombioe.2020.105838.

[12] X. Wang, H. Song, S. Ma, M. Li, G. He, M. Xie, X. Guo, Template ion-exchange synthesis of Co-Ni composite hydroxides nanosheets for supercapacitor with unprecedented rate capability, Chemical Engineering Journal. 432 (2022) 134319. https://doi.org/10.1016/j.cej.2021.134319.

[13] C. Wang, B. Yan, J. Zheng, L. Feng, Z. Chen, Q. Zhang, T. Liao, J. Chen, S. Jiang, C. Du, S. He, Recent progress in template-assisted synthesis of porous carbons for supercapacitors, Advanced Powder Materials. 1 (2022) 100018. https://doi.org/10.1016/j.apmate.2021.11.005.

[14] M. Vinayagam, R. Suresh Babu, A. Sivasamy, A.L.F. de Barros, Biomass-derived porous activated carbon nanofibers from Sapindus trifoliatus nut shells for high-performance symmetric supercapacitor applications, Carbon Letters. 31 (2021) 1133–1143. https://doi.org/10.1007/s42823-021-00235-4.

[15] G.M. Kalu-Uka, S. Kumar, A.C. Kalu-Uka, S. Vikram, G.O. Ihekweme, N. Ranjan, E.N. Anosike-Francis, G. Prajapati, A. Nduba, A.P. Onwualu, S. Kumar, Production of Activated Carbon Electrode for Energy Storage Application in Supercapacitors via KOH Activation of Waste Termite Biomass, Waste Biomass Valorization. 13 (2022) 2689–2704. https://doi.org/10.1007/s12649-022-01680-6.

[16] Z. Li, X. Ge, C. Li, S. Dong, R. Tang, C. Wang, Z. Zhang, L. Yin, Z. Li, X. Ge, C. Li, S. Dong, R. Tang, C. Wang, Z. Zhang, L. Yin, Rational Microstructure Design on Metal–Organic Framework Composites for Better Electrochemical Performances: Design Principle, Synthetic Strategy, and Promotion Mechanism, Small Methods. 4 (2020) 1900756. https://doi.org/10.1002/smtd.201900756.

[17] C. Kang, L. Ma, Y. Chen, L. Fu, Q. Hu, C. Zhou, Q. Liu, Metal-organic framework derived hollow rod-like NiCoMn ternary metal sulfide for high-performance

asymmetric supercapacitors, Chemical Engineering Journal. 427 (2022) 131003. https://doi.org/10.1016/j.cej.2021.131003.

[18] R. Vinodh, Y. Sasikumar, H.J. Kim, R. Atchudan, M. Yi, Chitin and chitosan based biopolymer derived electrode materials for supercapacitor applications: A critical review, Journal of Industrial and Engineering Chemistry. 104 (2021) 155–171. https://doi.org/10.1016/j.jiec.2021.08.019.

[19] N.N. Loganathan, V. Perumal, B.R. Pandian, R. Atchudan, T.N.J.I. Edison, M. Ovinis, Recent studies on polymeric materials for supercapacitor development, J Energy Storage. 49 (2022) 104149. https://doi.org/10.1016/j.est.2022.104149.

[20] H. Klefer, M. Munoz, A. Modrow, B. Böhringer, P. Wasserscheid, B.J.M. Etzold, Polymer-Based Spherical Activated Carbon as Easy-to-Handle Catalyst Support for Hydrogenation Reactions, Chem Eng Technol. 39 (2016) 276–284. https://doi.org/10.1002/ceat.201500445.

[21] M.M. Abdelaal, T.-C. Hung, S.G. Mohamed, C.-C. Yang, T.-F. Hung, Two Birds with One Stone: Hydrogel-Derived Hierarchical Porous Activated Carbon toward the Capacitive Performance for Symmetric Supercapacitors and Lithium-Ion Capacitors, ACS Sustain Chem Eng. 10 (2022) 4717–4727. https://doi.org/10.1021/acssuschemeng.2c00266.

[22] L. Wu, P. Wang, X. Chen, J. Zhang, H. Luo, Study of the preparation and electrochemical performance of porous carbon derived from hypercrosslinked polymers, Carbon Letters. 1 (2022) 1–14. https://doi.org/10.1007/s42823-022-00322-0.

[23] M.G. Mohamed, M.M.M. Ahmed, W.T. Du, S.W. Kuo, Meso/Microporous Carbons from Conjugated Hyper-Crosslinked Polymers Based on Tetraphenylethene for High-Performance CO2 Capture and Supercapacitor, Molecules 2021, Vol. 26, Page 738. 26 (2021) 738. https://doi.org/10.3390/molecules26030738.

[24] M.G. Mohamed, A.F.M. El-Mahdy, T.S. Meng, M.M. Samy, S.W. Kuo, Multifunctional Hypercrosslinked Porous Organic Polymers Based on Tetraphenylethene and Triphenylamine Derivatives for High-Performance Dye Adsorption and Supercapacitor, Polymers 2020, Vol. 12, Page 2426. 12 (2020) 2426. https://doi.org/10.3390/polym12102426.

[25] I. Kim, R. Vinodh, C.V.V.M. Gopi, H.-J. Kim, R.S. Babu, C. Deviprasath, M. Devendiran, S. Kim, Novel porous carbon electrode derived from hypercross-linked polymer of poly(divinylbenzene-co-vinyl benzyl chloride) for supercapacitor applications, J Energy Storage. 43 (2021) 103287. https://doi.org/10.1016/j.est.2021.103287.

[26] P. Bai, W. Liu, C. Yang, S. Wei, L. Xu, Boosting electrochemical performance of activated carbon by tuning effective pores and synergistic effects of active species, J Colloid Interface Sci. 587 (2021) 290–301. https://doi.org/10.1016/j.jcis.2020.12.022.

[27] I.I. Gurten Inal, Z. Aktas, Enhancing the performance of activated carbon based scalable supercapacitors by heat treatment, Appl Surf Sci. 514 (2020) 145895. https://doi.org/10.1016/j.apsusc.2020.145895.

[28] R. Vinodh, C.V.V.M. Gopi, V.G.R. Kummara, R. Atchudan, T. Ahamad, S. Sambasivam, M. Yi, I.M. Obaidat, H.J. Kim, A review on porous carbon electrode material derived from hypercross-linked polymers for supercapacitor applications, J Energy Storage. 32 (2020) 101831. https://doi.org/10.1016/j.est.2020.101831.

[29] O.P. Nanda, S. Badhulika, Biomass derived Nitrogen, Sulphur, and Phosphorus self-doped micro-meso porous carbon for high-energy symmetric supercapacitor – With a detailed study of the effect of different current collectors, J Energy Storage. 56 (2022) 106042. https://doi.org/10.1016/j.est.2022.106042.

[30] A. Gopalakrishnan, S. Badhulika, Effect of self-doped heteroatoms on the performance of biomass-derived carbon for supercapacitor applications, J Power Sources. 480 (2020) 228830. https://doi.org/10.1016/j.jpowsour.2020.228830.

[31] Y. Gao, Q. Wang, G. Ji, A. Li, J. Niu, Doping strategy, properties and application of heteroatom-doped ordered mesoporous carbon, RSC Adv. 11 (2021) 5361–5383. https://doi.org/10.1039/d0ra08993a.

[32] R. Vinodh, R.S. Babu, C.V.V.M. Gopi, C. Deviprasath, R. Atchudan, L.M. Samyn, A.L.F. de Barros, H.J. Kim, M. Yi, Influence of annealing temperature in nitrogen doped porous carbon balls derived from hypercross-linked polymer of anthracene for supercapacitor applications, J Energy Storage. 28 (2020) 101196. https://doi.org/10.1016/j.est.2020.101196.

[33] H. Quan, W. Tao, Y. Wang, D. Chen, Enhanced supercapacitor performance of Camellia oleifera shell derived hierarchical porous carbon by carbon quantum dots, J Energy Storage. 55 (2022) 105573. https://doi.org/10.1016/j.est.2022.105573.

[34] R. Atchudan, T.N. Jebakumar Immanuel Edison, S. Perumal, R. Vinodh, R.S. Babu, A.K. Sundramoorthy, A.A. Renita, Y.R. Lee, Facile synthesis of nitrogen-doped porous carbon materials using waste biomass for energy storage applications, Chemosphere. 289 (2022) 133225. https://doi.org/10.1016/j.chemosphere.2021.133225.

[35] X. Lin, S. Yin, W. Zhang, X. Li, N/P/O doped porous carbon materials for supercapacitor with high performance, Diam Relat Mater. 125 (2022) 109025. https://doi.org/10.1016/j.diamond.2022.109025.

[36] S. Breitenbach, A. Lumetzberger, M.A. Hobisch, C. Unterweger, S. Spirk, D. Stifter, C. Fürst, A.W. Hassel, Supercapacitor Electrodes from Viscose-Based Activated Carbon Fibers: Significant Yield and Performance Improvement Using Diammonium Hydrogen Phosphate as Impregnating Agent, C — Journal of Carbon Research. 6 (2020) 17. https://doi.org/10.3390/c6020017.

[37] J. Feng, W. Song, L. Sun, L. Xu, One-step nanocasting synthesis of nitrogen and phosphorus dual heteroatom doped ordered mesoporous carbons for supercapacitor application, RSC Adv. 6 (2016) 110337–110343. https://doi.org/10.1039/c6ra22728g.

[38] K. Wang, Y. Chen, Y. Liu, H. Zhang, Y. Shen, Z. Pu, H. Qiu, Y. Li, Plasma boosted N, P, O co-doped carbon microspheres for high performance Zn ion hybrid

supercapacitors, J Alloys Compd. 901 (2022) 163588. https://doi.org/10.1016/j.jallcom.2021.163588.

[39] Z.J. Zhang, B. Han, K.Y. Zhao, M.H. Gao, Z.Q. Wang, X.M. Yang, X.Y. Chen, Surface modification of carbon materials by nitrogen/phosphorus co-doping as well as redox additive of ferrous ion for cooperatively boosting the performance of supercapacitors, Ionics (Kiel). 26 (2020) 3027–3039. https://doi.org/10.1007/s11581-019-03406-6.

[40] R. Ragavan, A. Pandurangan, Exploration on magnetic and electrochemical properties of nitrogen and phosphorus Co-doped ordered mesoporous carbon for supercapacitor applications, Microporous and Mesoporous Materials. 338 (2022) 111959. https://doi.org/10.1016/j.micromeso.2022.111959.

[41] X. Li, Z. Lv, M. Wu, X. Li, Z. Li, N, P co-doped porous carbon from cross-linking cyclophosphazene for high-performance supercapacitors, Journal of Electroanalytical Chemistry. 881 (2021) 114952. https://doi.org/10.1016/j.jelechem.2020.114952.

[42] J. Zhu, Q. Zhang, H. Chen, R. Zhang, L. Liu, J. Yu, Setaria Viridis-Inspired Electrode with Polyaniline Decorated on Porous Heteroatom-Doped Carbon Nanofibers for Flexible Supercapacitors, ACS Appl Mater Interfaces. 12 (2020) 43634–43645. https://doi.org/10.1021/acsami.0c10933.

[43] F. Yang, S. Zhang, Y. Yang, W. Liu, M. Qiu, Y. Abbas, Z. Wu, D. Wu, Heteroatoms doped carbons derived from crosslinked polyphosphazenes for supercapacitor electrodes, Electrochim Acta. 328 (2019) 135064. https://doi.org/10.1016/j.electacta.2019.135064.

[44] D.T. Bakhoum, K.O. Oyedotun, S. Sarr, N.F. Sylla, V.M. Maphiri, N.M. Ndiaye, B.D. Ngom, N. Manyala, A study of porous carbon structures derived from composite of cross-linked polymers and reduced graphene oxide for supercapacitor applications, J Energy Storage. 51 (2022) 104476. https://doi.org/10.1016/j.est.2022.104476.

[45] F. Barzegar, V. Pavlenko, M. Zahid, A. Bello, X. Xia, N. Manyala, K.I. Ozoemena, Q. Abbas, Tuning the Nanoporous Structure of Carbons Derived from the Composite of Cross-Linked Polymers for Charge Storage Applications, ACS Appl Energy Mater. 4 (2021) 1763–1773. https://doi.org/10.1021/acsaem.0c02908.

[46] Y. Wen, L. Zhang, J. Liu, X. Wen, X. Chen, J. Ma, T. Tang, E. Mijowska, Hierarchical porous carbon sheets derived on a MgO template for high-performance supercapacitor applications, Nanotechnology. 30 (2019) 295703. https://doi.org/10.1088/1361-6528/ab0ee0.

[47] X. Xu, K. Sielicki, J. Min, J. Li, C. Hao, X. Wen, X. Chen, E. Mijowska, One-step converting biowaste wolfberry fruits into hierarchical porous carbon and its application for high-performance supercapacitors, Renew Energy. 185 (2022) 187–195. https://doi.org/10.1016/j.renene.2021.12.040.

[48] Y. Zhu, Z. Li, Y. Tao, J. Zhou, H. Zhang, Hierarchical porous carbon materials produced from heavy bio-oil for high-performance supercapacitor electrodes, J Energy Storage. 47 (2022) 103624. https://doi.org/10.1016/j.est.2021.103624.

[49] G. Li, Y. Li, X. Chen, X. Hou, H. Lin, L. Jia, One step synthesis of N, P co-doped hierarchical porous carbon nanosheets derived from pomelo peel for high performance supercapacitors, J Colloid Interface Sci. 605 (2022) 71–81. https://doi.org/10.1016/j.jcis.2021.07.065.

[50] N. Bu Gday, Serdar Altın, Sedat Yasar, Yasar Altın, Porous carbon prepared by zeolitic imidazolate framework (ZIF-7-III) as the precursor for supercapacitor applications in different electrolytes, Int J Energy Res. 46 (2022) 795–809. https://doi.org/10.1002/er.7204.

[51] S. Chakrabartty, B.K. Barman, C. Retna Raj, Nitrogen and phosphorous co-doped graphitic carbon encapsulated ultrafine OsP 2 nanoparticles: a pH universal highly durable catalyst for hydrogen evolution reaction, Chemical Communications. 55 (2019) 4399–4402. https://doi.org/10.1039/c9cc00822e.

[52] N. Wang, C. Wang, L. He, Y. Wang, W. Hu, S. Komarneni, Incomplete phase separation strategy to synthesize P/N co-doped porous carbon with interconnected structure for asymmetric supercapacitors with ultra-high power density, Electrochim Acta. 298 (2019) 717–725. https://doi.org/10.1016/j.electacta.2018.12.145.

[53] F. Mo, H. Zhang, Y. Wang, C. Chen, X. Wu, Heteroatom-doped hierarchical porous carbon for high performance flexible all-solid-state symmetric supercapacitors, J Energy Storage. 49 (2022) 104122. https://doi.org/10.1016/j.est.2022.104122.

[54] D. Meng, C. Wu, Y. Hu, Y. Jing, X. Zhang, S. Mahmud, S.P. Su, J. Zhu, Ingenious synthesis of chitosan-based porous carbon supercapacitors with large specific area by a small amount of potassium hydroxide, J Energy Storage. 51 (2022) 104341. https://doi.org/10.1016/j.est.2022.104341.

[55] L. Xu, Y. Xi, W. Li, Z. Hua, J. Peng, J. Hu, J.J. Zhou, P. Zhang, J. Wang, W. Wang, H. Ding, W. Wang, W. Ji, Y. Yang, X. Xu, L. Chen, X. Li, 3D frame-like architecture of N-C-incorporated mixed metal phosphide boosting ultrahigh energy density pouch-type supercapacitors, Nano Energy. 91 (2022) 106630. https://doi.org/10.1016/j.nanoen.2021.106630.

[56] S. Ntakirutimana, W. Tan, M.A. Anderson, Y. Wang, Editors' Choice-Review-Activated Carbon Electrode Design: Engineering Trade off with Respect to Capacitive Deionization Performance, Journal of the Electro. 167 (2020) 143501. https://doi.org/10.1149/1945-7111/abbfd7.

[57] Z. Guo, J. Zhang, H. Liu, Y. Kang, Development of a nitrogen-functionalized carbon adsorbent derived from biomass waste by diammonium hydrogen phosphate activation for Cr (VI) removal, Powder Technol. 318 (2017) 459–464. https://doi.org/10.1016/j.powtec.2017.06.024.

[58] P. Xu, J. Tong, L. Zhang, Y. Yang, X. Chen, J. Wang, S. Zhang, Dung beetle forewing-derived nitrogen and oxygen self-doped porous carbon for high performance solid-state supercapacitors, J Alloys Compd. 892 (2022) 162129. https://doi.org/10.1016/j.jallcom.2021.162129.

[59] X. Pang, M. Cao, J. Qin, X. Li, X. Yang, Synthesis of bamboo-derived porous carbon: exploring structure change, pore formation and supercapacitor application, Journal of Porous Materials. 29 (2022) 559–569. https://doi.org/10.1007/s10934-021-01181-2.

[60] N. Deka, J. Deka, G.K. Dutta, Nitrogen-Doped Porous Carbon Derived from Carbazole-Substituted Tetraphenylethylene-Based Hypercrosslinked Polymer for High-Performance Supercapacitor, ChemistrySelect. 3 (2018) 8483–8490. https://doi.org/10.1002/slct.201801507.

[61] W. Chen, M. Gong, K. Li, M. Xia, Z. Chen, H. Xiao, Y. Fang, Y. Chen, H. Yang, H. Chen, Insight into KOH activation mechanism during biomass pyrolysis: Chemical reactions between O-containing groups and KOH, Appl Energy. 278 (2020) 115730. https://doi.org/10.1016/j.apenergy.2020.115730.

[62] Z. Guo, J. Fan, J. Zhang, Y. Kang, H. Liu, L. Jiang, C. Zhang, Sorption heavy metal ions by activated carbons with well-developed microporosity and amino groups derived from Phragmites australis by ammonium phosphates activation, J Taiwan Inst Chem Eng. 58 (2016) 290–296. https://doi.org/10.1016/j.jtice.2015.05.041.

[63] L. Liu, Y. Li, S. Fan, Preparation of KOH and H3PO4 Modified Biochar and Its Application in Methylene Blue Removal from Aqueous Solution, Processes 2019, Vol. 7, Page 891. 7 (2019) 891. https://doi.org/10.3390/pr7120891.

[64] J. Cui, Z.X. Zhang, H. Quan, Y. Hu, S. Wang, D. Chen, Effect of various ammonium salts as activating additive on the capacitance performance of hierarchical porous carbon derived from camellia husk, J Energy Storage. 51 (2022) 104347. https://doi.org/10.1016/j.est.2022.104347.

[65] Z. Wang, Y. Tan, Y. Yang, X. Zhao, Y. Liu, L. Niu, B. Tichnell, L. Kong, L. Kang, Z. Liu, F. Ran, Pomelo peels-derived porous activated carbon microsheets dual-doped with nitrogen and phosphorus for high performance electrochemical capacitors, J Power Sources. 378 (2018) 499–510. https://doi.org/10.1016/j.jpowsour.2017.12.076.

[66] A. Marcilla, M.I. Beltran, A. Gómez-Siurana, I. Martinez-Castellanos, D. Berenguer, V. Pastor, A.N. García, TGA/FTIR study of the pyrolysis of diammonium hydrogen phosphate–tobacco mixtures, J Anal Appl Pyrolysis. 112 (2015) 48–55. https://doi.org/10.1016/j.jaap.2015.02.023.

[67] Z. Lin, J. Zhu, P. Zhang, L. Deng, N/P co-doped porous carbon microspheres for supercapacitor with long-term electrochemical stability, J Mater Res. 36 (2021) 1250–1261. https://doi.org/10.1557/s43578-021-00210-9.

[68] X. Xie, J. Shi, Y. Pu, Z. Wang, L.L. Zhang, J.X. Wang, D. Wang, Cellulose derived nitrogen and phosphorus co-doped carbon-based catalysts for catalytic reduction of p-nitrophenol, J Colloid Interface Sci. 571 (2020) 100–108. https://doi.org/10.1016/j.jcis.2020.03.035.

[69] Y. Zhang, Q. Sun, K. Xia, B. Han, C. Zhou, Q. Gao, H. Wang, S. Pu, J. Wu, Facile Synthesis of Hierarchically Porous N/P Codoped Carbon with Simultaneously High-Level Heteroatom-Doping and Moderate Porosity for High-Performance

Supercapacitor Electrodes, ACS Sustain Chem Eng. 7 (2019) 5717–5726. https://doi.org/10.1021/acssuschemeng.8b05024.

[70] Y. Ma, D. Wu, T. Wang, D. Jia, Nitrogen, Phosphorus Co-doped Carbon Obtained from Amino Acid Based Resin Xerogel as Efficient Electrode for Supercapacitor, ACS Appl Energy Mater. 3 (2020) 957–969. https://doi.org/10.1021/acsaem.9b02032.

[71] Z. Hu, S. Li, P. Cheng, W. Yu, R. Li, X. Shao, W. Lin, D. Yuan, N, P-co-doped carbon nanowires prepared from bacterial cellulose for supercapacitor, J Mater Sci. 51 (2016) 2627–2633. https://doi.org/10.1007/s10853-015-9576-x.

[72] J. Li, X. Yun, Z. Hu, L. Xi, N. Li, H. Tang, P. Lu, Y. Zhu, Three-dimensional nitrogen and phosphorus co-doped carbon quantum dots/reduced graphene oxide composite aerogels with a hierarchical porous structure as superior electrode materials for supercapacitors, J Mater Chem A Mater. 7 (2019) 26311–26325. https://doi.org/10.1039/c9ta08151h.

[73] G. Li, Y. Li, J. Deng, H. Lin, X. Hou, L. Jia, Ultrahigh rate capability supercapacitors based on tremella-like nitrogen and phosphorus co-doped graphene, Mater Chem Front. 4 (2020) 2704–2715. https://doi.org/10.1039/d0qm00392a.

[74] C. Wang, Y. Zhou, L. Sun, P. Wan, X. Zhang, J. Qiu, Sustainable synthesis of phosphorus- and nitrogen-co-doped porous carbons with tunable surface properties for supercapacitors, J Power Sources. 239 (2013) 81–88. https://doi.org/10.1016/j.jpowsour.2013.03.126.

[75] H. Liu, W. Fan, H. Lv, W. Zhang, J. Shi, M. Huang, S. Liu, H. Wang, N, P-Doped Carbon-Based Freestanding Electrodes Enabled by Cellulose Nanofibers for Superior Asymmetric Supercapacitors, ACS Appl Energy Mater. 4 (2021) 2327–2338. https://doi.org/10.1021/acsaem.0c02859.

[76] J. Yi, Y. Qing, C.T. Wu, Y. Zeng, Y. Wu, X. Lu, Y. Tong, Lignocellulose-derived porous phosphorus-doped carbon as advanced electrode for supercapacitors, J Power Sources. 351 (2017) 130–137. https://doi.org/10.1016/j.jpowsour.2017.03.036.

[77] A. Daraghmeh, S. Hussain, I. Saadeddin, L. Servera, E. Xuriguera, A. Cornet, A. Cirera, A Study of Carbon Nanofibers and Active Carbon as Symmetric Supercapacitor in Aqueous Electrolyte: A Comparative Study, Nanoscale Res Lett. 12 (2017) 1–10. https://doi.org/10.1186/s11671-017-2415-z.

[78] Y. Shu, Q. Bai, G. Fu, Q. Xiong, C. Li, H. Ding, Y. Shen, H. Uyama, Hierarchical porous carbons from polysaccharides carboxymethyl cellulose, bacterial cellulose, and citric acid for supercapacitor, Carbohydr Polym. 227 (2020) 115346. https://doi.org/10.1016/j.carbpol.2019.115346.

[79] M. Khandelwal, C. Van Tran, J. Bin In, Nitrogen and phosphorous Co-Doped Laser-Induced Graphene: A High-Performance electrode material for supercapacitor applications, Appl Surf Sci. 576 (2022) 151714. https://doi.org/10.1016/j.apsusc.2021.151714.

[80] W. Zheng, Z. Li, G. Han, Q. Zhao, G. Lu, X. Hu, J. Sun, R. Wang, C. Xu, Nitrogen-doped activated porous carbon for 4.5 V lithium-ion capacitor with high energy and

power density, J Energy Storage. 47 (2022) 103675. https://doi.org/10.1016/j.est.2021.103675.

[81] M. Yang, Q. Kong, W. Feng, W. Yao, Q. Wang, Hierarchical porous nitrogen, oxygen, and phosphorus ternary doped hollow biomass carbon spheres for high-speed and long-life potassium storage, Carbon Energy. 4 (2022) 45–59. https://doi.org/10.1002/cey2.157.

[82] E.S. Goda, A. ur Rehman, B. Pandit, A. Al-Shahat Eissa, S. Eun Hong, K. Ro Yoon, Al-doped Co9S8 encapsulated by nitrogen-doped graphene for solid-state asymmetric supercapacitors, Chemical Engineering Journal. 428 (2022) 132470. https://doi.org/10.1016/j.cej.2021.132470.

[83] B. Tiwari, A. Joshi, M. Munjal, G. Kaur, R.K. Sharma, G. Singh, Synergistic combination of N/P dual-doped activated carbon with redox-active electrolyte for high performance supercapacitors, Journal of Physics and Chemistry of Solids. 161 (2022) 110449. https://doi.org/10.1016/j.jpcs.2021.110449.

[84] D. Mohapatra, O. Muhammad, M.S. Sayed, S. Parida, J.-J. Shim, In situ nitrogen-doped carbon nano-onions for ultrahigh-rate asymmetric supercapacitor, Electrochim Acta. 331 (2020) 135363. https://doi.org/10.1016/j.electacta.2019.135363.

[85] T. Liu, S. Ali, Z. Lian, C. Si, D.S. Su, B. Li, Phosphorus-doped onion-like carbon for CO 2 electrochemical reduction: the decisive role of the bonding configuration of phosphorus, J Mater Chem A Mater. 6 (2018) 19998–20004. https://doi.org/10.1039/c8ta06649c.

[86] I. Palm, E. Kibena-Põldsepp, U. Mäeorg, J. Kozlova, M. Käärik, A. Kikas, J. Leis, V. Kisand, A. Tamm, K. Tammeveski, Silicon carbide-derived carbon electrocatalysts dual doped with nitrogen and phosphorus for the oxygen reduction reaction in an alkaline medium, Electrochem Commun. 125 (2021) 106976. https://doi.org/10.1016/j.elecom.2021.106976.

[87] S.K. Ramasahayam, Z. Hicks, T. Viswanathan, Thiamine-Based Nitrogen, Phosphorus, and Silicon Tri-doped Carbon for Supercapacitor Applications, ACS Sustain Chem Eng. 3 (2015) 2194–2202. https://doi.org/10.1021/acssuschemeng.5b00453.

[88] J. Chen, Y. Cheng, Q. Zhang, C. Luo, H.-Y. Li, Y. Wu, H. Zhang, X. Wang, H. Liu, X. He, J. Han, D.-L. Peng, M. Liu, M.-S. Wang, J. Chen, Y. Cheng, Q. Zhang, C. Luo, H. Zhang, J. Han, D. Peng, M. Wang, H. Li, X. Wang, Y. Wu, H. Liu, X. He, M. Liu, Designing and Understanding the Superior Potassium Storage Performance of Nitrogen/Phosphorus Co-Doped Hollow Porous Bowl-Like Carbon Anodes, Adv Funct Mater. 31 (2021) 2007158. https://doi.org/10.1002/adfm.202007158.

[89] L. Wang, X. Ma, Preparation of N, P self-doped activated carbon hollow fibers derived from liquefied wood, Wood Sci Technol. 55 (2021) 83–93. https://doi.org/10.1007/s00226-020-01244-8.

[90] H. Liu, M. Wang, D.D. Zhai, X.Y. Chen, Z.J. Zhang, Design and theoretical study of carbon-based supercapacitors especially exhibiting superior rate capability by the

synergistic effect of nitrogen and phosphor dopants, Carbon N Y. 155 (2019) 223–232. https://doi.org/10.1016/j.carbon.2019.08.066.

[91] N.F. Sylla, S. Sarr, N.M. Ndiaye, B.K. Mutuma, A. Seck, B.D. Ngom, M. Chaker, N. Manyala, Enhanced Electrochemical Behavior of Peanut-Shell Activated Carbon/Molybdenum Oxide/Molybdenum Carbide Ternary Composites, Nanomaterials. 11 (2021) 1056. https://doi.org/10.3390/nano11041056.

[92] C. Zhao, Y. Ding, Y. Huang, N. Li, Y. Hu, C. Zhao, Soybean root-derived N, O co-doped hierarchical porous carbon for supercapacitors, Appl Surf Sci. 555 (2021) 149726. https://doi.org/10.1016/j.apsusc.2021.149726.

[93] M. Mansuer, L. Miao, D. Zhu, H. Duan, Y. Lv, L. Li, M. Liu, L. Gan, Facile construction of highly redox active carbons with regular micropores and rod-like morphology towards high-energy supercapacitors, Mater Chem Front. 5 (2021) 3061–3072. https://doi.org/10.1039/d0qm01101k.

[94] K. Ramadass, C.I. Sathish, G. Singh, S.M. Ruban, A.M. Ruban, R. Bahadur, G. Kothandam, T. Belperio, J. Marsh, A. Karakoti, J. Yi, A. Vinu, Morphologically tunable nanoarchitectonics of mixed kaolin-halloysite derived nitrogen-doped activated nanoporous carbons for supercapacitor and CO2 capture applications, Carbon N Y. 192 (2022) 133–144. https://doi.org/10.1016/j.carbon.2022.02.047.

[95] Y. Ma, D. Wu, T. Wang, D. Jia, Nitrogen, Phosphorus Co-doped Carbon Obtained from Amino Acid Based Resin Xerogel as Efficient Electrode for Supercapacitor, ACS Appl Energy Mater. 3 (2020) 957–969. https://doi.org/10.1021/acsaem.9b02032.

[96] Y. Wang, B. Yang, D. Zhang, H. Shi, M. Lei, H. Li, K. Wang, Strong polar nonaqueous solvent-assisted microwave fabrication of N and P co-doped microporous carbon for high-performance supercapacitor, Appl Surf Sci. 512 (2020) 145711. https://doi.org/10.1016/j.apsusc.2020.145711.

[97] M. Jiang, W. Xu, X. Du, X. Yang, F. Wang, Y. Zhou, Y. Pan, Y. Lu, N, P,O-doped porous carbon electrode material derived from lignin modified chitosan xerogel for supercapacitor, Materials Today Sustainability. 22 (2023) 100372. https://doi.org/10.1016/j.mtsust.2023.100372.

[98] X. Zhang, G. Yan, H. Li, Z. Li, J. Chen, L. Wang, Y. Wu, Slit needleless electrospun heteroatoms-doped hollow porous carbon nanofibers for solid-state flexible supercapacitors, J Alloys Compd. 943 (2023) 169188. https://doi.org/10.1016/j.jallcom.2023.169188.

[99] A. Gopalakrishnan, S. Badhulika, From onion skin waste to multi-heteroatom self-doped highly wrinkled porous carbon nanosheets for high-performance supercapacitor device, J Energy Storage. 38 (2021) 102533. https://doi.org/10.1016/j.est.2021.102533.

[100] J. Chen, H. Wei, H. Chen, W. Yao, H. Lin, S. Han, N/P co-doped hierarchical porous carbon materials for superior performance supercapacitors, Electrochim Acta. 271 (2018) 49–57. https://doi.org/10.1016/j.electacta.2018.03.129.

[101] H. Bi, X. He, H. Zhang, H. Li, N. Xiao, J. Qiu, N, P co-doped hierarchical porous carbon from rapeseed cake with enhanced supercapacitance, Renew Energy. 170 (2021) 188–196. https://doi.org/10.1016/j.renene.2021.01.099.

[102] Y. Lu, J. Liang, S. Deng, Q. He, S. Deng, Y. Hu, D. Wang, Hypercrosslinked polymers enabled micropore-dominant N, S Co-Doped porous carbon for ultrafast electron/ion transport supercapacitors, Nano Energy. 65 (2019) 103993. https://doi.org/10.1016/j.nanoen.2019.103993.

[103] O. Fasakin, J.K. Dangbegnon, D.Y. Momodu, M.J. Madito, K.O. Oyedotun, M.A. Eleruja, N. Manyala, Synthesis and characterization of porous carbon derived from activated banana peels with hierarchical porosity for improved electrochemical performance, Electrochim Acta. 262 (2018) 187–196. https://doi.org/10.1016/j.electacta.2018.01.028.